

**DESIGNING NOVEL DENO_x CATALYSTS WITH A WIDE
THERMAL OPERATIONAL WINDOW**

A THESIS SUBMITTED TO
THE GRADUATE SCHOOL OF ENGINEERING AND SCIENCE
OF BILKENT UNIVERSITY
IN PARTIAL FULFILLMENT OF THE REQUIREMENTS FOR
THE DEGREE OF
MASTER OF SCIENCE
IN
CHEMISTRY

By
Merve Tohumeken

June 2016

DESIGNING NOVEL DENO_x CATALYSTS WITH A WIDE THERMAL
OPERATIONAL WINDOW

By Merve Tohumeken

June 2016

We certify that we have read this thesis and that in our opinion it is fully adequate,
in scope and in quality, as a thesis for the degree of Master of Science.

Emrah Özensoy (Advisor)

Ömer Dağ

Nuray Oktar

Approved for the Graduate School of Engineering and Science:

Levent Onural

Director of the Graduate School

ABSTRACT

DESIGNING NOVEL DENO_x CATALYSTS WITH A WIDE THERMAL OPERATIONAL WINDOW

Merve Tohumeken
M.S. in Chemistry
Advisor: Emrah Özensoy
June 2016

The main objective of this study is to design novel DeNO_x catalyst to widen the operational temperature range of exhaust emission control systems. For this purpose, single and multi NO_x-storage domains (*e.g.* K₂O, BaO) were loaded on an Al₂O₃/ZrO₂/TiO₂ (AZT) ternary mixed oxide support with various compositions and different catalytic systems were synthesized by utilizing sol-gel and wetness impregnation methods. These materials were characterized by means of XRD, N₂ sorption, *in-situ* FTIR and TPD measurements in comparison to the Pt/20Ba/Al benchmark catalyst. K₂O and BaO co-loading on AZT sample reveals better platinum dispersion than that of the single storage domain materials. Particularly, Pt/5.4K-8Ba/AZT system revealed promising NO_x storage capacity (NSC) and high sulfur removal performance. NO_x/SO_x adsorption geometries and stabilities of the generated adsorbates were analyzed using *in-situ* FTIR and TPD. Although the Pt/20Ba/AZT and Pt/10K/AZT catalysts revealed high NSC, they showed poor sulfur regeneration characteristics. In conclusion, it was demonstrated that K₂O and BaO co-impregnated samples can be utilized to design new catalytic architectures to modify the operational temperature window of exhaust emission control catalysts.

Keywords: NSR/DeNO_x catalysts, Al₂O₃/ZrO₂/TiO₂, K₂O, BaO, Pt, NO_x storage capacity, sulfur poisoning.

ÖZET

GENİŞ SICAKLIK ARALIĞINDA ÇALIŞABİLEN YENİ NESİL DeNO_x KATALİZÖRLERİNİN TASARIMI

Merve Tohumeken
Kimya, Yüksek Lisans
Tez Danışmanı: Emrah Özensoy
Haziran 2016

Bu çalışmanın temel amacı, geniş sıcaklık aralığında çalışabilen yeni nesil DeNO_x katalizörlerini dizayn etmek ve bu katalizörlerin fonksiyonel ve karakteristik özelliklerini incelemektir. Bu amaç için, tek yada çoklu (NO_x depolayıcı) bazik oksitler çeşitli oranlarda Al₂O₃/ZrO₂/TiO₂ üçlü metal oksitin üzerine eklendi ve ıslak emdirme ve sol-gel yöntemleri kullanılarak farklı katalizör sistemleri elde edildi. XRD, N₂ tutma, FTIR and TPD deneyleri ile bu katalizör sistemlerinin fonksiyonel ve karakteristik özellikleri incelendi ve referans katalizör olarak kullanılan Pt/20Ba/Al ile karşılaştırıldı. Bu deneylerin sonuçları ışığında, K₂O and BaO oksitlerinin AZT malzemesi üzerine birlikte eklenmesi, tekli yüklemelere kıyasla katalizörün üzerinde daha iyi platin metali dağılımı sağlamaktadır. Pt/5.4K-8Ba/AZT malzemesi optimum NO_x depolama kapasitesine sahiptir ayrıca bu malzemenin kükürt zehirlenmesine karşı yüksek dirence sahip olduğu gözlenmiştir. NO_x/SO_x gazlarının yüzeye tutunma geometrileri ve dayanıklılığı FTIR ve TPD deneyleri ile ölçüldü. Pt/20Ba/AZT ve Pt/10K/AZT katalizörleri yüksek NO_x depolama kapasitesine sahiptir ama kükürt zehirlenmesinde verimli performansları yoktur. Sonuç olarak, BaO ve K₂O

malzemelerini birlikte ekleme metodu geniş aralıklarda çalışabilen yeni nesil katalizörlerini tasarlamada kullanılabileceği saptanmıştır.

Anahtar sözcükler: NSR/DeNO_x katalizörleri, Al₂O₃/ZrO₂/TiO₂, K₂O, BaO, Pt, NO_x depolama kapasitesi, kükürt zehirlenmesi.

Acknowledgement

First and foremost, I would like to express the deepest gratitude to my advisor Assoc. Prof. Emrah Özensoy. He enabled me to gain a broad scientific perspective, let me be part of his research group, and patiently followed my maturation and completion of this work. I would like to thank him for his knowledge, encouragement, supervision, patience and guidance throughout my studies.

I also would like to thank especially to Zafer Say for sharing his knowledge, collaboration and the precious time that he has shared with me through my undergraduate and graduate studies. I would like to express my sincere appreciations to Zehra Aybegüm Samast for valuable scientific discussions and emotional support. I wish to thank to Pelin Paşabeyoğlu for her support and encouragement.

I want to express my thanks to our group members Kerem Emre Ercan, Deniz Erdoğan, Merve Kurt, Merve Balcı, Mustafa Çağlayan, Mustafa Karatok, and Elif Perşembe. We shared lots of memories in the Özensoy group.

I also wish to acknowledge chemistry department members, Gülbahar Saat, Pınar Alsaç, Ethem Anber, Fadime Balcı, Deniz Gökçeaslan who have provided my memories.

During all the time in Bilkent, I have been very pleased to be with you, Irmak Özferendeci, Betül Turgut, Selge Çatlı and Zeynep Türel.

I also would like to acknowledge TUBITAK for financial support.

I am immeasurably indebted to my two huge families which have constantly supported and encouraged me during my graduate study. ‘The Kunt and Tohumeken Family.’ Especially to my husband, Şehmus Tohumeken for his continuous support and unconditional love.

I also want to thank two little cuties Berra and Betül Kunt.

Dedicated to my son Said Musa

Contents

| | |
|---|----|
| Chapter 1 | 1 |
| Introduction..... | 1 |
| 1.1 Emissions of Air Pollutants from Transport | 1 |
| 1.2 General Information about NO _x Storage Reduction Catalysts..... | 3 |
| 1.3 NSR Reaction Mechanism | 5 |
| 1.4 Components of NSR Catalysts..... | 7 |
| 1.5 Deactivation Mechanism of NSR Catalysts | 9 |
| 1.6 Aim of the Present Study | 10 |
| Chapter 2 | 11 |
| Experimental | 11 |
| 2.1 Sample Preparation | 11 |
| 2.1.1 Synthesis of Ternary Oxides: Pt/Al ₂ O ₃ /ZrO ₂ /TiO ₂ | 11 |
| 2.1.2 Synthesis of Pt/ K ₂ O/ Al ₂ O ₃ /ZrO ₂ /TiO ₂ Samples | 12 |
| 2.1.3 Synthesis of Pt/BaO/Al ₂ O ₃ /ZrO ₂ /TiO ₂ Samples | 13 |
| 2.1.4 Synthesis of Pt/K ₂ O-BaO /Al ₂ O ₃ /ZrO ₂ /TiO ₂ Samples..... | 13 |
| 2.2 Instrumentation | 14 |
| 2.2.1 XRD and Specific Surface Area Analysis | 14 |

| | |
|--|----|
| 2.2.2 <i>In-situ</i> FTIR Spectroscopy and Temperature Programmed Desorption Analysis..... | 15 |
| 2.3 Experimental Procedures | 17 |
| 2.3.1 NO _x Adsorption <i>via in-situ</i> FTIR..... | 17 |
| 2.3.2 NO _x Reduction <i>via in-situ</i> FTIR | 17 |
| 2.3.3 SO _x Adsorption <i>via in-situ</i> FTIR..... | 18 |
| 2.3.4 SO _x Reduction <i>via in-situ</i> FTIR | 18 |
| 2.3.5 NO _x Desorption <i>via</i> TPD..... | 18 |
| 2.3.6 SO _x Desorption <i>via</i> TPD | 19 |
| Chapter 3 | 20 |
| Results and Discussion..... | 20 |
| 3.1 Structural Characterization of the Materials | 20 |
| 3.1.1 XRD Analysis | 20 |
| 3.1.2 BET Analysis | 23 |
| 3.2 In situ FTIR Analysis | 26 |
| 3.2.1 NO _x Adsorption Analysis..... | 26 |
| 3.2.1.1 NO _x Adsorption Analysis of Single Storage Domain Materials | 26 |
| 3.2.1.2 NO _x Adsorption Analysis of Multi Storage Domain Materials | 28 |
| 3.2.2 NO _x Reduction Analysis | 31 |
| 3.2.2.1 NO _x Reduction Analysis of Single Storage Domain Materials | 32 |

| | |
|---|----|
| 3.2.2.2 NO _x Reduction Analysis of Multi Storage Domain Materials..... | 34 |
| 3.2.3 SO _x Adsorption Analysis | 37 |
| 3.2.3.1 SO _x Adsorption Analysis of Single Storage Domain Materials..... | 38 |
| 3.2.3.2 SO _x Adsorption Analysis of Multi Storage Domain Materials..... | 41 |
| 3.2.4 SO _x Reduction Analysis | 43 |
| 3.2.4.1 SO _x Reduction Analysis of Single Storage Domain Materials | 44 |
| 3.2.4.2 SO _x Reduction Analysis of Multi Storage Domain Materials | 46 |
| 3.3 TPD Analysis | 48 |
| 3.3.1 NO _x TPD Analysis | 48 |
| 3.3.1.1 NO _x TPD Analysis Single Storage Domain Materials..... | 51 |
| 3.3.1.2 NO _x TPD Analysis of Multi Storage Domain Materials | 56 |
| 3.3.2 SO _x TPD Analysis..... | 60 |
| 3.3.2.1 SO _x TPD Analysis of Single Storage Domain Materials | 61 |
| 3.3.2.2 SO _x TPD Analysis of Multi Storage Domain Materials..... | 65 |
| Chapter 4 | 69 |
| Conclusion | 69 |
| Bibliography..... | 72 |

List of Figures

| | |
|--|----|
| Figure 1 : Contribution of the transport sector to the total emissions of main air pollutants (Copyright notice © European Environment Agency, 2014[2].)..... | 2 |
| Figure 2 : The mortality rate from air pollution varied among WHO regions and the distribution of deaths attributable to air pollution by disease type (Copyright notice © World Health Organization, 2016[4].)..... | 3 |
| Figure 3 : Schematic illustration of the general operation principle of NSR catalysts (Copyright © 2011 Elsevier. Reproduced with permission from ref [21])...... | 5 |
| Figure 4: Schematic diagram of in situ FTIR and TPD analysis system [47]...... | 16 |
| Figure 5 : XRD patterns of the Pt/AZT, Pt/8Ba/AZT, Pt/20Ba/AZT and Pt/20Ba/Al (benchmark) catalysts calcined at 973 K. | 21 |
| Figure 6 : XRD patterns of the Pt/AZT, Pt/2.7K/AZT, Pt/5.4K/AZT and Pt/20Ba/Al (benchmark) catalysts calcined at 973 K. | 22 |
| Figure 7 : XRD patterns of the Pt/2.7K-8BaAZT, Pt/2.7K-20Ba/AZT, Pt/5.4K-8Ba/AZT and Pt/5.4K-20Ba/AZT catalysts calcined at 973 K..... | 23 |
| Figure 8 : BET specific surface area values for the Pt/AZT, Pt/8Ba/AZT, Pt/20Ba/AZT catalysts and Pt/20Ba/Al benchmark catalyst after calcination at 973 K..... | 24 |
| Figure 9 : BET specific surface area values for the Pt/AZT, Pt/2.7K/AZT, Pt/5.4K/AZT catalysts and Pt/20Ba/Al benchmark catalyst after calcination at 973 K..... | 25 |

| | |
|---|----|
| Figure 10 : BET specific surface area values for the K ₂ O –BaO co-impregnated Pt/2.7K-8Ba/AZT, Pt/2.7K-20Ba/AZT, Pt/5.4K-8Ba/AZT and Pt/5.4K-20Ba/AZT catalysts after calcination at 973K. | 26 |
| Figure 11 : <i>In-situ</i> FTIR spectra of stepwise NO ₂ (g) adsorption on activated a) Pt/AZT, b) Pt/8Ba/AZT and c) Pt/20Ba/AZT at 323 K. The topmost spectrum belongs to the saturated surfaces..... | 27 |
| Figure 12 : <i>In-situ</i> FTIR spectra of stepwise NO ₂ (g) adsorption on activated a) Pt/AZT, b) Pt/2.7K/AZT and c) Pt/5.4K/AZT at 323 K. The topmost spectrum belongs to saturated surface. | 28 |
| Figure 13 : <i>In-situ</i> FTIR spectra of stepwise NO ₂ (g) adsorption on activated a) Pt/AZT, b) Pt/8Ba/AZT, c) Pt/2.7K-8Ba/AZT and d) Pt/5.4K-8Ba/AZT at 323 K. The topmost spectrum belongs to saturated surface. | 30 |
| Figure 14 : <i>In-situ</i> FTIR spectra of stepwise NO ₂ (g) adsorption on activated a) Pt/AZT, b) Pt/20Ba/AZT, c) Pt/2.7K-20Ba/AZT and d) Pt/5.4K-20Ba/AZT at 323 K. The topmost spectrum belongs to saturated surface..... | 31 |
| Figure 15 : <i>In-situ</i> FTIR spectra of NO ₂ (g) reduction <i>via</i> H ₂ (g) on a) Pt/AZT, b) Pt/8Ba/AZT and c) Pt/20Ba/AZT. | 32 |
| Figure 16 : Schematic representation of nitrate reduction mechanism. (Copyright © 2014 Elsevier. Reproduced with permission from ref [68]). | 33 |
| Figure 17 : <i>In-situ</i> FTIR spectra of NO ₂ (g) reduction <i>via</i> H ₂ (g) on a) Pt/AZT, b) Pt/2.7K/AZT and c) Pt/5.4K/AZT. | 34 |
| Figure 18 : <i>In-situ</i> FTIR spectra of NO ₂ (g) reduction <i>via</i> H ₂ (g) on saturated a) Pt/AZT, b) Pt/8Ba/AZT, c) Pt/2.7K-8Ba/AZT and d) Pt/5.4.K-8Ba/AZT. | 36 |

Figure 19 : *In-situ* FTIR spectra of NO₂ (g) reduction *via* H₂ (g) on saturated a) Pt/AZT, b) Pt/20Ba/AZT, c) Pt/2.7K-20Ba/AZT and d) Pt/5.4.K-20Ba/AZT. 37

Figure 20 : *In-situ* FTIR spectra related to the SO_x uptake properties of a) Pt/AZT, b) Pt/8Ba/AZT, c) Pt/20Ba/AZT and d) Pt/20Ba/Al that are exposed to 2 Torr SO_x at 323 K, followed by annealing at 373, 473, 573 and 673 K in the presence of the SO_x gas mixture for 5 min..... 38

Figure 21 : *In-situ* FTIR spectra related to the SO_x uptake properties of a) Pt/AZT, b)Pt/2.7K/AZT, c)Pt/5.4K/AZT and d) Pt/10K/AZT exposed to 2 Torr SO_x at 323 K, followed by annealing at 373, 473, 573 and 673 K in the presence of SO_x gas mixture for 5 min (Copyright © 2016 Elsevier. Reproduced with permission from ref [49]). 39

Figure 22 : *In-situ* FTIR spectra related to SO_x uptake properties of a) Pt/AZT, b) Pt/8Ba/AZT, c) Pt/2.7K-8Ba/AZT and d) Pt/5.4K-8Ba/AZT exposed to 2 Torr SO_x at 323 K, followed by annealing at 373, 473, 573 and 673 K in the presence of SO_x gas mixture for 5 min. 41

Figure 23 : *In-situ* FTIR spectra related to SO_x uptake properties of a) Pt/AZT, b) Pt/20Ba/AZT, c) Pt/2.7K-20Ba/AZT and d) Pt/5.4K-20Ba/AZT that exposed to 2 Torr SO_x at 323 K, followed by annealing at 373, 473, 573 and 673 K in the presence of SO_x gas mixture for 5 min. 42

Figure 24 : *In-situ* FTIR spectra related to SO_x reduction properties of a) Pt/AZT, b) Pt/8Ba/AZT, c) Pt/20Ba/AZT and d) Pt/20Ba/Al samples *via* H₂ (g). The catalysts were initially poisoned by 2 Torr SO_x. After evacuation, poisoned samples were exposed to 15 Torr H₂ (g) at 323, 473, 673 and 773 K for 5 min. All spectra were acquired at 323 K. 44

Figure 25 : *In-situ* FTIR spectra related to SO_x reduction properties of a) Pt/AZT, b)Pt/2.7K/AZT, c)Pt/5.4K/AZT and d) Pt/10K/AZT samples via H₂ (g). The poisoned samples were exposed to 15 Torr H₂ (g) at 323, 473, 673, 773 and 873 K for 5 min. All spectra were acquired at 323 K(Copyright © 2016 Elsevier. Reproduced with permission from ref. Copyright 2016 Elsevier B.V. [49])...... 45

Figure 26 : *In-situ* FTIR spectra related to SO_x reduction properties of a) Pt/AZT, b) Pt/8Ba/AZT c) Pt/2.7K-8Ba/AZT, d) Pt/5.4K-8Ba/AZT and samples via H₂ (g). The poisoned samples were exposed to 15 Torr H₂ (g) at 323, 473, 673, 773 and 873 K for 5 min. All spectra were acquired at 323 K. 46

Figure 27 : *In-situ* FTIR spectra related to SO_x reduction properties of a) Pt/AZT, b) Pt/20Ba/AZT c) Pt/2.7K-20Ba/AZT, d) Pt/5.4K-20Ba/AZT and samples via H₂ (g). The poisoned samples were exposed to 15 Torr H₂ (g) at 323, 473, 673, 773 and 873 K for 5 min. All spectra were acquired at 323 K. 47

Figure 28 : NO_x TPD profiles for a) Pt/AZT, b) Pt/8Ba/AZT c) Pt/20Ba/AZT, d) Pt/20Ba/Al samples after saturation with 5 Torr NO₂ (g) at 323 K for 10 min. The inset spectra in each panel represent *in-situ* FTIR spectra before (black) and after (red) TPD analysis..... 51

Figure 29 : Surface area normalized NSC values of BaO loaded AZT catalysts obtained from integrated NO_x TPD signals. 53

Figure 30 : NO_x TPD profiles for a) Pt/AZT, b) Pt/2.7K/AZT c) Pt/5.4K/AZT, d) Pt/10K/AZT samples after saturation with 5 Torr NO₂ (g) at 323 K for 10 min. The inset spectra in each panel represent *in-situ* FTIR spectra before (black) and after (red) TPD analysis..... 54

| | |
|---|----|
| Figure 31 : Surface area normalized NSC values of K ₂ O loaded AZT catalysts obtained from integrated NO _x TPD signals. | 55 |
| Figure 32 : NO _x TPD profiles for a) Pt/AZT, b) Pt/8Ba/AZT c) Pt/2.7K-8Ba/AZT, d) Pt/5.4K-8Ba/AZT samples after saturation with 5 Torr NO ₂ (g) at 323 K for 10 min. The inset spectra in each panel represent in-situ FTIR spectra before (black) and after (red) TPD analysis. | 56 |
| Figure 33 : Surface area normalized NSC values of K ₂ O-BaO co-loaded AZT catalysts containing 8 wt.% BaO obtained from integrated NO _x TPD signals..... | 57 |
| Figure 34 : NO _x TPD profiles for a) Pt/AZT, b) Pt/20Ba/AZT c) Pt/2.7K-20Ba/AZT, d) Pt/5.4K-20Ba/AZT samples after saturation with 5 Torr NO ₂ (g) at 323 K for 10 min. The inset spectra in each panel represent <i>in-situ</i> FTIR spectra before (black) and after (red) TPD analysis. | 58 |
| Figure 35 : Surface area normalized NSC values of K ₂ O-BaO co-loaded AZT catalysts containing 20 wt.% BaO obtained from integrated NO _x TPD signals... | 59 |
| Figure 36 : Surface area normalized relative “NO _x -slip” values of K ₂ O-BaO co-loaded AZT catalysts at T < 573 K, containing 20 wt.% BaO obtained from integrated NO _x TPD signals. | 60 |
| Figure 37 : SO _x TPD profiles for a) Pt/AZT, b) Pt/8Ba/AZT c) Pt/20Ba/AZT, d) Pt/20Ba/Al samples after 2 Torr SO _x adsorption at 673 K for 30 min. | 61 |
| Figure 38 : <i>In-situ</i> FTIR spectra corresponding to residual sulfur content on Pt/AZT, Pt/8Ba/AZT, Pt/20Ba/AZT and Pt/20Ba/Al samples before (black) and after (red) SO _x TPD experiments. | 62 |
| Figure 39 : TPD profiles for a) Pt/AZT, b) Pt/2.7K/AZT c) Pt/5.4K/AZT, d) Pt/10K/AZT samples after 2 Torr SO _x adsorption at 673 K for 30 min. | 63 |

| | |
|--|----|
| Figure 40 : <i>In-situ</i> FTIR spectra corresponding to residual sulfur content on Pt/AZT, Pt/2.7K/AZT, Pt/5.4K/AZT and Pt/10K/AZT samples before (black) and after (red) SO _x TPD experiment..... | 64 |
| Figure 41 : TPD profiles for a) Pt/AZT, b) Pt/8Ba/AZT c) Pt/2.7K-8Ba/AZT, d) Pt/5.4K-8Ba/AZT samples after 2 Torr SO _x adsorption at 673 K for 30 min. | 65 |
| Figure 42 : FTIR spectra corresponding to residual sulfur content on Pt/AZT, Pt/8Ba/AZT, Pt/2.7K-8Ba/AZT and Pt/5.4K-8Ba/AZT and samples before (black) and after (red) SO _x TPD experiments. | 66 |
| Figure 43 : TPD profiles for a) Pt/AZT, b) Pt/20Ba/AZT c) Pt/2.7K-20Ba/AZT, d) Pt/5.4K-20Ba/AZT samples after 2 Torr SO _x adsorption at 673 K for 30 min. ... | 67 |
| Figure 44 : <i>In-situ</i> FTIR spectra corresponding to residual sulfur content on Pt/AZT, Pt/20Ba/AZT, Pt/2.7K-20Ba/AZT and Pt/5.4K-20Ba/AZT and samples before (black) and after (red) SO _x TPD experiments..... | 68 |

List of Table

| | |
|---|---|
| Table 1 : Vibrational frequencies of NO_3^- and NO_2^- in inorganic coordination compounds (Copyright © 2003 Wiley. Reproduced with permission from ref [34]). | 7 |
|---|---|

List of Abbreviations

BET: Brunauer-Emmett-Teller

EDX: Energy-Dispersive X-ray spectroscopy

FTIR: Fourier Transform Infrared Spectroscopy

IR: Infrared

JCPDS: Joint Committee on Powder Diffraction Standards

NIST: National Institute of Standards and Technology

NO_x: Nitrogen Oxides (e.g. N₂O, NO, NO₂)

NSR: NO_x Storage and Reduction

NSC: NO_x Storage Capacity

PGM: Platinum Group Metal

PID: Proportional Integral Derivative

RT: Room Temperature

QMS: Quadruple Mass Spectrometer

SCR: Selective Catalytic Reduction

SO_x: Sulfur Oxides (e.g. SO₂, SO₃)

SSA: Specific Surface Area

TPD: Temperature Programmed Desorption

Chapter 1

Introduction

1.1 Emissions of Air Pollutants from Transport

Union of Concerned Scientists states that more than half of the carbon monoxide (CO) and nitrogen oxides (NO_x), and almost a quarter of the hydrocarbons are emitted into air by vehicles in 2013[1]. Air pollution causes serious risks for human health and the environment. Some of the major pollutants that are generated by mobile sources are particulate matter (PM), hydrocarbons, carbon monoxide, nitric oxide, sulfur dioxide and non-methane volatile organic compounds (NMVOC) and other greenhouse gases. Diesel exhaust is the major contributor of PM pollution, which threatens the human health the most by penetrating deeply into lung tissue and causing various respiratory diseases[1]. Hydrocarbons irritate the respiratory system and reduce oxygen intake capacity while nitrogen oxide causes lung irritation, pneumonia and influenza, affecting the immune system[1].

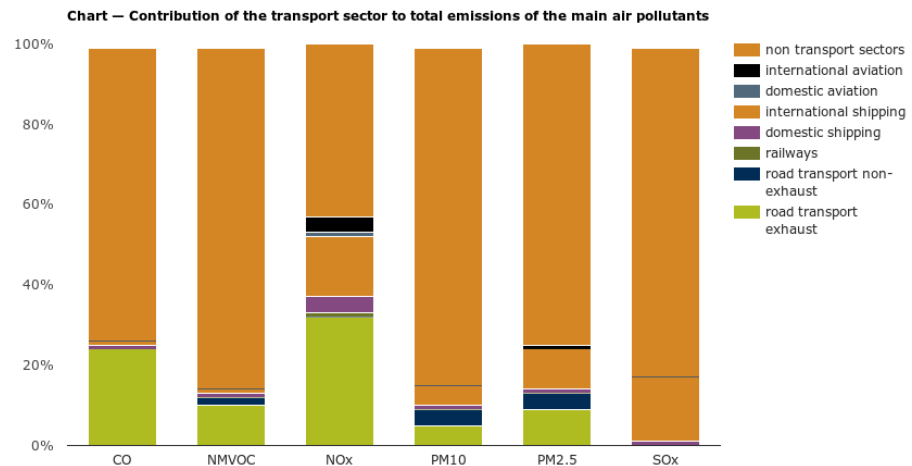


Figure 1 : Contribution of the transport sector to the total emissions of main air pollutants (Copyright notice © European Environment Agency, 2014[2].)

Figure 1 demonstrates the contribution of transportation to the emission of air pollutants published by European Environment Agency (EEA)[2]. Transportation sector achieved important emission reductions in the 1990-2012 period. These reductions were mostly in CO and NMVOC emissions, which decreased both by 81 % together with NO_x (33 %), SO_x (26 %) and particulates[2]. However, these emission reductions should be continuously sustained to minimize severe environmental and health implications.

World Health Organization (WHO) committee reported that ambient air pollution (from traffic, industrial sources, and residual of fuel combustion) caused 3.0 million deaths in 2012[3].

Air pollution also causes cardiovascular diseases, stroke, chronic obstructive pulmonary disease and lung cancer, as well as increasing the risks for

respiratory infections. Figure 2 shows the distribution of deaths attributable to air pollution by disease type[4].

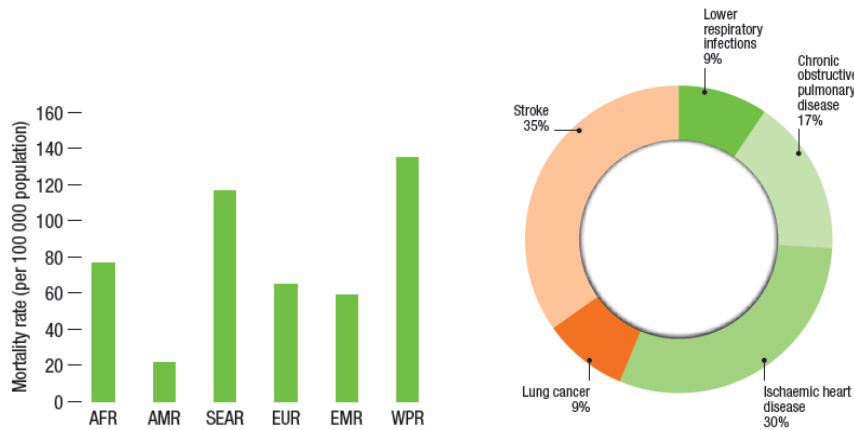


Figure 2 : The mortality rate from air pollution varied among WHO regions and the distribution of deaths attributable to air pollution by disease type (Copyright notice © World Health Organization, 2016[4].)

1.2 General Information about NO_x Storage Reduction Catalysts

Gasoline engines operate under stoichiometric conditions with an air to fuel ratio (A/F) of 14.7[5]. Three way catalysts (TWC) work efficiently for this A/F to reduce NO_x from exhaust gases. Lean-burn gasoline and diesel engines are more preferable due to their lower fuel consumption and CO₂ emission [6-9]. However, these engines operate with A/F in the range of 20:1 to 65:1[6, 10, 11]. Due to the presence of excess oxygen, TWCs are inefficient to reduce NO_x in the diesel exhaust emission [6, 7, 12].

NO_x gases emitted from the mobile sources have devastating effects on environment, atmosphere and especially human health since they cause acid rain,

ozone smog and eutrophication [13]. Klingstedt *et al.* reported that half of the total global toxic emissions was generated by mobile vehicles. Thus, stringent limitations were introduced for the regulation of mobile emission sources [14]. Recently, it was reported that some of the existing diesel engine cars in the market exceeded the NO_x emission limits by more than 20 times [15].

To control NO_x emissions from mobile engines, new technologies were innovated. Some of the emission control technologies include direct decomposition of NO_x, selective catalytic reduction (SCR) of NO_x and NO_x storage reduction (NSR) systems [12]. Direct decomposition of NO_x is favorable at elevated temperatures and require very high activation energies, which cannot be attained in mobile applications [16]. SCR technology can be utilized in three different forms: i) hydrocarbon-SCR, ii) plasma assisted-SCR and iii) ammonia (urea)-SCR [17, 18]. Urea-SCR is the most commonly used technology, while it presents various important challenges such as injection problems, continuous control and refilling of the urea tank *etc* [19]. NO_x Storage Reduction (NSR) technology innovated by Toyota Motor Company is a promising technology as it does not require any external reducing agents [20]. This technology is comprised of two main catalytic cycles, which are the NO_x storage and the NO_x reduction cycles. In the storage cycle (*i.e.* lean cycle), NO is oxidized to NO₂ on precious metal active sites (*e.g.* Pt) and then NO₂ is stored on basic storage sites. In the reduction cycle (*i.e.* rich cycle), stored NO_x is removed from storage sites and reduced to N₂ on precious metal sites. NSR catalysts operate in a cyclic manner by switching between lean and rich conditions (Figure 3).

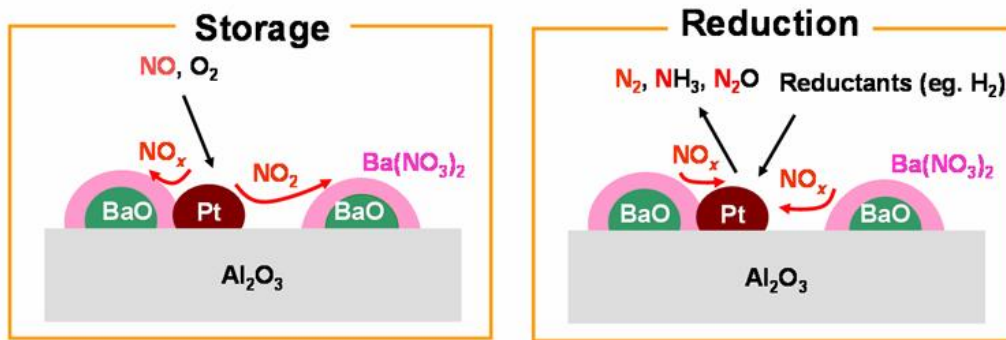


Figure 3 : Schematic illustration of the general operation principle of NSR catalysts (Copyright © 2011 Elsevier. Reproduced with permission from ref [21]).

1.3 NSR Reaction Mechanism

Despite a vast number of previously published reports, role of each of the catalytic components in NSR systems and the interaction between these components are still under debate[12, 22]. Furthermore, the mechanism of the NSR catalyst (storage and reduction process) is also not entirely clear. There exist a number of formerly proposed NO_x storage mechanisms on surface of the catalyst. One of the proposed mechanisms for the NO oxidation process includes the following steps [23, 24]:



As shown above, NO is oxidized on Pt metal surface to NO₂ and it does not directly take part in the NO_x trapping process. Although this proposed mechanism is promising for NO oxidation process, an undefined rate determining step is still unclear [25, 26]. Furthermore, Olsson *et al.* reported that a vacant Pt site (reaction 1 and 4) and oxidation of the metallic Pt sites (PtO and PtO₂) decrease the NO oxidation activity[27, 28].

In order to explain the role of the basic metal oxide (*e.g.* BaO) sites in the NO_x storage process, Olsson *et al.* suggested a reaction pathway as follows [29, 30]:



It is also worth mentioning that BaO can store NO₂ more effectively than NO[31].

Furthermore, nitric oxide reacts with the surface oxygen of oxides to yield nitrite and nitrate compounds[32, 33]. Their spectral identifications can be carried out by analogy with corresponding spectra of inorganic complexes in Table 1. The variations in nitrite/nitrate adsorption geometries reflects the differences in surface properties. Also, corresponding IR spectra reflect the differences in the ionic-covalent properties of the metal-oxygen bonds on the surface[34].

Table 2.21. Stretching vibration frequencies of NO_3^- and NO_2^- in inorganic coordination compounds.

| Structure | ν_3 (cm^{-1}) | ν_1 (cm^{-1}) |
|------------------|------------------------------|--|
| NO_3^- | 1380 | 1050 ^a |
| | 1530–1480 | 1290–1250 1035–970 |
| | 1565–1500 | 1300–1260 1040–1010 |
| | 1650–1600 | 1225–1170 1030–1000 |
| Structure | ν_s (cm^{-1}) | ν_{as} (cm^{-1}) |
| NO_2^- | 1260 | 1330 |
| | 1220–1205 | |
| | 1440–1335 | 1350–1315 |
| M-O-N=O | 1470–1450 | 1065–1050 |
| | 1520–1390 | 1260–1180 |

^aForbidden in the IR spectrum.

Table 1 : Vibrational frequencies of NO_3^- and NO_2^- in inorganic coordination compounds (Copyright © 2003 Wiley. Reproduced with permission from ref [34]).

1.4 Components of NSR Catalysts

Typical NSR catalysts consist of three main components; these are platinum group metals, NO_x storage components and support metal oxides. Pt/20Ba/Al sample containing 1 wt. %Pt and 20wt. % BaO on $\gamma\text{-Al}_2\text{O}_3$ is known as the conventional benchmark catalyst. As a platinum group metal (PGM) component, Pt metal is commonly used in both oxidation and reduction processes. As mentioned earlier, on the active platinum surface, NO is oxidized and stored under lean conditions and under rich conditions, NO_x is reduced to N_2 .

Basic oxides such as BaO, K₂O, SrO and CeO₂ can be used as storage components in NSR catalysts. In the current work, BaO and K₂O were exploited to synthesize complex NSR catalysts. BaO is commonly used as the conventional storage material, but this material is not efficient in NO_x storage at $T \geq 673$ K [35-38]. On the other hand, K₂O is capable of storing NO_x at $T \geq 573$ K [39, 40]. In the current study, both BaO or K₂O are utilized simultaneously to expand the thermal operational window of NSR systems [39].

As a support metal oxide, alumina (Al₂O₃) is commonly used due to its high SSA and thermal stability. Furthermore, alumina has also NO_x storage capability and improves NSC of NSR systems [39].

In this work, instead of alumina, a novel Al₂O₃/ZrO₂/TiO₂ (AZT) ternary mixed oxide was used. Since, BaO reacts with Al₂O₃ to form BaAl₂O₄ causing a decreasing the NSC, using AZT is an attempt to prevent the formation of such unwanted phases. TiO₂ is used because of its high tolerance against sulfur poisoning due to its higher surface acidity than alumina [20, 41-43]. The interaction between TiO₂ and BaO samples causes the formation of inactive BaTiO_x phases. In order to avoid such phenomena, ZrO₂ is used as a solid diffusion barrier between TiO₂ and BaO.

1.5 Deactivation Mechanism of NSR Catalysts

Sulfur poisoning and thermal aging are some of the most prominent deactivation mechanisms that affect the long-term performance of NSR catalysts.

NO_x and SO_x are both acidic gases, thus they compete with each other for the adsorption sites on the basic oxide surfaces. It is known that BaSO_4 ($\Delta G(\text{BaSO}_4) = 56.89$ kJ/mol) has a very high thermodynamic stability compared to that of $\text{Ba}(\text{NO}_3)_2$ ($\Delta G(\text{Ba}(\text{NO}_3)_2) = 13.31$ kJ/mol) [44]. Hence, BaSO_4 formation suppresses the NO_x adsorption and NO_x storage capacity (NSC) of the catalyst is decreased [45-47]. $\text{Al}_2(\text{SO}_4)_3$ is also formed upon sulfur poisoning. $\text{Al}_2(\text{SO}_4)_3$ can plug the pores of the catalyst and suppresses the availability of active sites, and decreases the performance of the NSR catalysts[20]. Although sulfur concentration in diesel fuel has been significantly reduced over the recent years (*e.g.* Ultra Low Sulfur Diesel, ULSD has only 15 ppm of total sulfur content), complete removal of sulfur is still a technological and financial challenge for the petroleum refining industry.

In order to recover the catalyst surface and keep NSR performance stable, the sulfated surface should be regenerated. For this purpose, sample is heated to high temperatures (*e.g.* > 873 K). While heating the sample, thermal aging of the catalyst can occur. In addition, under rich conditions, oxidation of the reducing agent (*i.e.* hydrocarbon, CO and H_2) generates heat on the surface of the catalyst and causes thermal aging. Such exothermic processes also results in the agglomeration of Pt particles and significant loss of Pt surface area [12, 48].

1.6 Aim of the Present Study

This study will mainly focus on investigating the effect of utilizing multiple basic oxides on the NSC of NSR systems. BaO based catalysts are very sensitive to sulfur species. Sulfur removal performance of the NSR catalysts can also be improved by using K₂O (*ca.* 650 K) as the thermodynamic stability of sulfates on K₂O is lower than that of BaO (*ca.* 750 K) [20, 49]. Furthermore, the basicity of the NO_x storage component is directly related to the NO_x trapping performance. Different basic oxide NSC performances were investigated at various temperatures and found out to be increasing in the following order: K > Ba > Sr > Na > Ca > Li [12, 50]. Thus in the current work, K₂O is selected in attempt to improve the sulfur removal performance as well as the NSC.

Another important motivation of this work is that conventional benchmark catalyst (Pt/BaO/Al) is efficient in NO_x adsorption and storage within 473-673 K, but gasoline direct injection engines can operate at temperatures above 673 K. At these elevated temperatures, conventional benchmark catalyst cannot perform effectively [51]. Hence, simultaneous utilization of K₂O and BaO can be effective in NSR applications [52]. A noteworthy advantage of K₂O based catalysts is also associated to their stronger basicity and prevention of the formation of the undesired BaAl₂O₄ species in concomitant with their enhanced NSC at 523-823 K [53].

Chapter 2

Experimental

2.1 Sample Preparation

2.1.1 Synthesis of Ternary Oxides: Pt/Al₂O₃/ZrO₂/TiO₂

The Pt/Al₂O₃/ZrO₂/TiO₂ mixed oxides were synthesized using a sol-gel method. For this synthesis protocol, aluminum sec-butoxide (Sigma Aldrich, ACS Reagent, 97%) precursor was initially dissolved in 30 mL of 2-propanol (Sigma Aldrich, ACS Reagent >99.5%) and stirred for 10 min under ambient conditions. Then, titanium (IV) isopropoxide (Sigma Aldrich, ACS Reagent, 97%) and 20 mL of 2-propanol were added to the solution and stirred for 10 min. After zirconium (IV) propoxide (Sigma Aldrich, ACS Reagent, 70 wt. % in 1-propanol) and 50 mL of 2-propanol were added, the slurry was stirred for 10 min under ambient conditions. In order to obtain gel formation of ternary oxides, 9 mL of 0.5 M nitric acid solution (Sigma Aldrich, ACS Reagent, 65%) were added in a dropwise fashion. Before calcination in air at 973 K, material was dried under ambient condition for 48 h. The nominal composition of the synthesized material by weight was Al₂O₃:ZrO₂:TiO₂ = 50:35:15 and this material will be abbreviated as AZT throughout the text.

Pt/AZT material was synthesized by incipient wetness impregnation method. Calcined AZT ternary oxide was dispersed in 50 mL deionized water and a solution

of $\text{Pt}(\text{NH}_3)_2(\text{NO}_2)_2$ (Aldrich, diamminedinitritoplatinum (II), 3.4 wt. % solution in dilute NH_3 (aq)) was added to the solution. This material was stirred at 340 K for 8 h and followed by calcination at 973 K for 150 min to remove the organic functionalities in the precursors. The nominal Pt loading in the final material by weight was calculated to be 1 wt. %. For the synthesis of 3 g of the Pt/AZT catalyst, 1.43 mL of platinum precursor was utilized.

2.1.2 Synthesis of Pt/ K_2O / Al_2O_3 / ZrO_2 / TiO_2 Samples

The K_2O -based catalysts were prepared by incipient wetness impregnation method. Calcined AZT support material and potassium nitrate precursor ($\text{KNO}_3 \cdot 6\text{H}_2\text{O}$, >99.0%, Fluka, France) were mixed in 50 mL deionized water. This mixture was stirred at 340 K for 8 h. Then, material was calcined at 973 K for 150 min. For the synthesis of the 3 g of the catalyst with different K_2O loadings, 0.174 g, 0.347 g or 0.644 g potassium precursor were used to obtain K_2O loadings of 2.7, 5.4, 10 wt. %, respectively. Finally, these catalysts were functionalized with the platinum precursor to have a nominal Pt loading of 1 wt. %. In the last step of the preparation, platinum loaded catalysts were calcined at 973 K for 150 min. Throughout the current text, K_2O -loaded (2.7, 5.4 and 10 wt. % K_2O) samples are abbreviated as Pt/2.7K/AZT, Pt/5.4K/AZT and Pt/10K/AZT respectively.

2.1.3 Synthesis of Pt/BaO/Al₂O₃/ZrO₂/TiO₂ Samples

Similar to the K₂O-based materials, BaO based catalysts were also prepared by employing the incipient wetness impregnation method. Pt/BaO/Al₂O₃/ZrO₂/TiO₂ catalysts with 8 and 20 wt. % BaO loadings were prepared via impregnating the calcined AZT support material with an aqueous solution of barium nitrate (Ba(NO₃)₂, ACS Reagent, ≥99%, Riedel-de Häen, Germany). For the synthesis of the Pt/8Ba/AZT and Pt/20Ba/AZT samples, initially 0.44 g and 1.28 g Ba(NO₃)₂ were dissolved in the deionized water and stirred for 10 min followed by the addition of AZT. Next, the solution was stirred at 340 K for 8 h. This step was followed by calcination at 873 K in air for 150 min. After calcination, mixed oxides were functionalized with 1 wt. % Pt as in the case of K₂O based materials. It should be noted that the molar amount of 2.7 and 5.4 wt. % K₂O were comparable to that of 8 and 20 wt. % BaO in AZT supported materials. In other words, the molar loading of the basic oxide used in the single storage domain materials (i.e. either BaO or K₂O) were rather similar.

2.1.4 Synthesis of Pt/K₂O-BaO /Al₂O₃/ZrO₂/TiO₂ Samples

For the synthesis of Pt/K₂O-BaO /Al₂O₃/ZrO₂/TiO₂, Ba(NO₃)₂ and KNO₃ were co-impregnated on AZT using an analogous synthesis method as described above. Pt/2.7K₂O-8BaO/AZT and Pt/5.4K₂O-8BaO/AZT, as well as Pt/2.7K₂O-20BaO/AZT and Pt/5.4K₂O-20BaO/AZT samples were prepared by wetness impregnation of calcined Al₂O₃/ZrO₂/TiO₂ support with the corresponding aqueous solutions of barium nitrate (Ba(NO₃)₂, ACS Reagent, ≥99%, Riedel-de Häen,

Germany) and potassium nitrate precursors ($\text{KNO}_3 \cdot 6\text{H}_2\text{O}$, >99.0%, Fluka, France). For the synthesis of 3 g of Pt/2.7 K₂O-8BaO/AZT and Pt/5.4K₂O- 8BaO/AZT, 0.174 g and 0.347 g of KNO₃ and 0.44 g Ba(NO₃)₂ precursors were used, respectively. Then, 50 mL of deionized water was added and stirred for 8 h at 340 K. This step was followed by calcination at 873 K in air for 150 min to remove nitrate/nitrite content by thermal decomposition. The same procedure was applied for the synthesis of the Pt/K₂O-20BaO/AZT catalysts. For the synthesis of 3 g of Pt/2.7 K₂O-20BaO/AZT and Pt/5.4K₂O-20BaO/AZT, 0.174 g and 0.347 g of KNO₃ and 1.28 g Ba(NO₃)₂ precursors were used, respectively. Next, these materials were impregnated with the proper amount of the Pt precursor in order to obtain a Pt loading of 1 wt. %. Finally, obtained samples were calcined in air at 973 K for structural stabilization. In the current text, Pt/2.7K₂O-8BaO/Al₂O₃/ZrO₂/TiO₂, Pt/5.4K₂O-8BaO/Al₂O₃/ZrO₂/TiO₂, Pt/2.7K₂O-20BaO/Al₂O₃/ZrO₂/TiO₂ and Pt/5.4K₂O-20BaO/Al₂O₃/ZrO₂/TiO₂ samples will be abbreviated as Pt/2.7K-8Ba/AZT, Pt/5.4K-8Ba/AZT, Pt/2.7K-20Ba/AZT and Pt/5.4K-20Ba/AZT; respectively.

2.2 Instrumentation

2.2.1 XRD and Specific Surface Area Analysis

Powder X-Ray Diffraction (XRD) analysis was performed using a Rigaku Miniflex diffractometer, equipped with a Miniflex goniometer and an X-Ray source with Cu $K\alpha$ radiation, at $\lambda = 1.5418 \text{ \AA}$, 30 kV and 15 mA. The powder sample was pressed onto a standard glass holder and scanned between 10-80° 2θ values with a

scan rate of 2 deg. min⁻¹. Assignment of the diffraction patterns were performed by using Joint Committee on Powder Diffraction Standards (JCPDS) cards.

Specific Surface Area (SSA) of the synthesized materials were measured by low temperature isothermal adsorption/desorption of N₂ via the five point Brunauer, Emmett, and Teller (BET) method. Before the measurement, the samples were dehydrated at 573 K for 2 h in vacuum. SSA analysis was performed by utilizing a Micromeritics ASAP2000 gas sorption and porosimetry system.

2.2.2 *In-situ* FTIR Spectroscopy and Temperature Programmed Desorption Analysis

In-situ Fourier Transform Infrared (FTIR) spectroscopic measurements were carried out in transmission mode in the batch type catalytic reactor [54] combined with an FTIR spectrometer (Bruker Tensor 27) and quadruple mass spectrometer (QMS, Stanford Research System, RGA200). Typically, 18-22 mg of powder samples were pressed onto a high conductance and lithographically-etched tungsten grid (Tech Etch, P/N PW10379- 003). A tantalum foil was also spot welded onto the W-grid to accommodate a K-type thermocouple (chromel and alumel having thickness of 0.015", Omega Engineering, Inc.) for temperature measurements. W-grid was connected to the copper legs together with an electrical vacuum feedthrough. Samples placed into the batch-mode reactor were initially baked out at 403 K for 12 h to remove water from the catalyst and the reactor walls. All FTIR spectra were acquired at 323 K by using a MCT (Hg-Cd-Te) MIR detector that was cooled with liquid nitrogen (LN₂) cooling. MKS Baratron Pressure Transducer

Type 626 gauge and wide range pressure gauge (EDVAC WRG-S-NW35) comprised of Piranyi and cold-cathode gauges were used to control gas pressures. Rotary and turbo pumps were used for removing the gases from the gas manifold and reactor system.

The QMS was used for the temperature programmed desorption (TPD) and Residual Gas Analysis (RGA) experiments. During the TPD experiments, sample was heated within the range of 323-1023 K with a linear temperature ramp rate of 12 K/min. The temperature ramp was controlled by using a computer controlled PID electronics (Gefran 600-DRRR) and an adjustable DC power supply.

Prior to the experiments, the sample surface was activated by flushing the reactor with 0.5 Torr NO_2 for 5 min followed by evacuation and annealing to 973K.

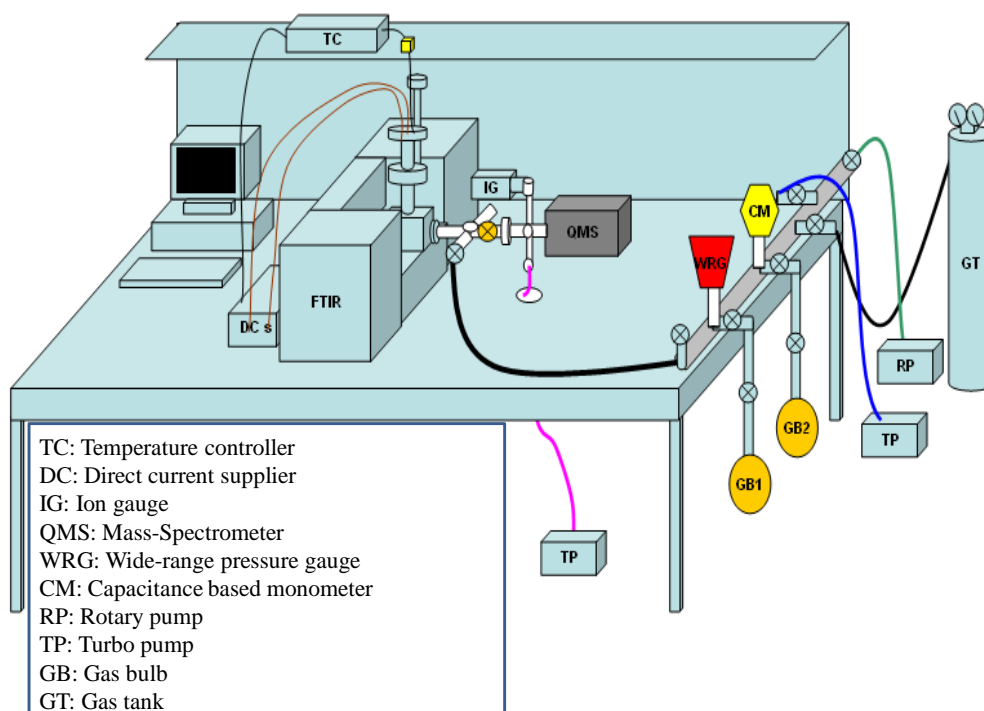


Figure 4: Schematic diagram of in situ FTIR and TPD analysis system [47].

2.3 Experimental Procedures

2.3.1 NO_x Adsorption *via in-situ* FTIR

To investigate NO_x adsorption properties of the synthesized catalysts, stepwise NO₂ (g) dosing experiments were performed by incrementally increasing the adsorbate exposure. NO₂ (g) was prepared by mixing NO (g) (Air Products, 99.9%) and excess O₂ (g) (Linde GmbH, Germany, 99.999%) followed by multiple freeze-pump-thaw cycles for purification. First, 0.5 Torr of NO₂ (g) were dosed into the manifold and released onto the sample for 1 min. Upon the expansion of the gas into the reactor, 0.05 Torr NO₂ (g) pressure were obtained over the sample. Before acquiring the FTIR spectrum, NO₂ (g) was pumped from the system until the pressure reached *ca.* 10⁻³ Torr. This procedure was repeated 10 times for each sample by using an initial NO₂ (g) pressure of 1 Torr in the manifold. As the final saturation step, 5 Torr NO₂ (g) was dosed over the sample for 10 min. All NO_x adsorption experiments were performed at 323 K.

2.3.2 NO_x Reduction *via in-situ* FTIR

NO_x reduction experiments were performed by exposing 15 Torr H₂ (g) (Linde GmbH, Germany, >99.9%) onto a NO₂-saturated sample surface at 323 K. Next, the time-dependent FTIR spectra were acquired at various times in the presence of H₂ (g) for a duration of 2 h. Then, the sample was heated to various temperatures up to 573 K in the presence of H₂ (g) for the complete reduction of adsorbed NO_x. All of the FTIR spectra were recorded after cooling the sample to 323 K.

2.3.3 SO_x Adsorption *via in-situ* FTIR

Sulfation experiments were performed by exposing the surfaces to a 2 Torr SO_x mixture for 5 min at 323 K. SO₂:O₂ (SO₂ purity >99%, Air Products, O₂ purity >99.999%, Linde GmbH) partial pressure ratio of the SO_x mixture was 1:10. After introduction of the SO_x mixture, the sample was heated to different temperatures within 323 – 673 K for 5 min. After each annealing step, the sample was cooled down to 323 K to record an FTIR spectrum. Each step was performed in the presence of the SO_x gas mixture. After the completion of the SO_x adsorption experiments, SO_x gas was evacuated from the system.

2.3.4 SO_x Reduction *via in-situ* FTIR

Prior to SO_x reduction experiments, the sample was sulfated as mentioned in the previous section. Subsequently, the sulfated catalyst was exposed to 15 Torr H₂ (g) (Linde GmbH, Germany, >99.9%) at 323 K for 5 min followed by heating under hydrogen atmosphere at 473, 673, 773, 873 and 973 K for 5 min. FTIR spectra were acquired after each annealing step in the presence of H₂ (g) at 323 K.

2.3.5 NO_x Desorption *via* TPD

For NO_x TPD experiments, the catalyst sample was initially exposed to 5 Torr NO₂ (g) at 323 K for 10 min followed by evacuation at <10⁻³ Torr. Then the sample was heated under vacuum with a constant rate of 12 K/min to 973 K. FTIR spectra were also acquired before and after TPD experiments. The desorbed NO_x species

during the TPD analysis were monitored by recording the QMS signals at $m/z = 18$, 28, 30, 32, 44, 46 corresponding to H_2O , N_2/CO , NO , O_2 , $\text{N}_2\text{O}/\text{CO}_2$, NO_2 species, respectively.

2.3.6 SO_x Desorption *via* TPD

In SO_x TPD analysis, each sample was initially saturated with a 2 Torr SO_x mixture at 673 K for 30 min. Then the system was evacuated to a pressure lower than 10^{-3} Torr. After evacuation, the sample was heated in vacuum to 1173 K with a linear heating rate of 12 K/min. Thermally desorbed SO_x species were monitored by QMS channels at $m/z=32$ (O_2) and $m/z= 64$ (SO_2).

Chapter 3

Results and Discussion

3.1 Structural Characterization of the Materials

3.1.1 XRD Analysis

XRD patterns of the Pt/AZT, Pt/8Ba/AZT, Pt/20Ba/AZT as well as the conventional benchmark Pt/20Ba/Al catalyst are given in a comparative fashion in Figure 5. As shown in Figure 5, the Pt/AZT material exhibits a highly amorphous structure with broad diffraction features, revealing sharp platinum diffraction signals (JCPDS 001-1190). Incorporation of baria on the Pt/AZT system does not alter the disordered nature of this surface. Furthermore, addition of baria to the Pt/AZT sample hinders the precious metal agglomeration and facilitates platinum particle dispersion.

In the XRD pattern of the Pt/20Ba/Al benchmark catalyst, there are two more crystalline phases, which can be assigned to γ -Al₂O₃ (JCPDS 001-1303) and undesired BaAl₂O₄ (JCPDS 017-0306). On the surface of the benchmark catalyst, BaO reacts with Al₂O₃ to form a BaAl₂O₄ structure resulting in the loss of the NO_x storage sites. Lack of the BaAl₂O₄ domains in the AZT-based catalysts could be a positive attribute suggesting that the NO_x storage sites can remain intact without forming inactive mixed oxide systems with the support.

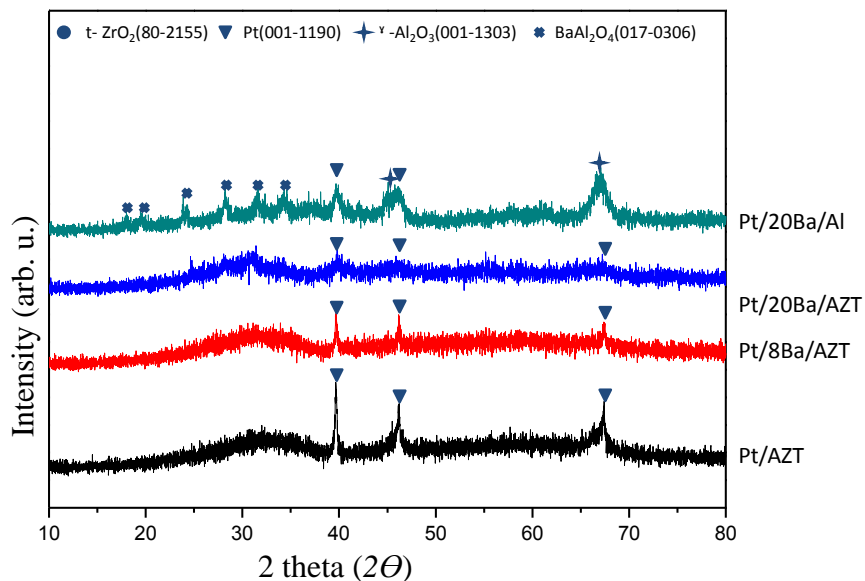


Figure 5 : XRD patterns of the Pt/AZT, Pt/8Ba/AZT, Pt/20Ba/AZT and Pt/20Ba/Al (benchmark) catalysts calcined at 973 K.

Figure 6 illustrates the XRD patterns of Pt/AZT, Pt/2.7K/AZT, Pt/5.4K/AZT and Pt/20Ba/Al recorded after calcination at 973 K. Incorporation of 2.7K/AZT and 5.4K/AZT does not reveal any additional phases except a small increase in the intensities of the Pt diffraction features suggesting that K_2O domains are rather disordered and small in particle size.

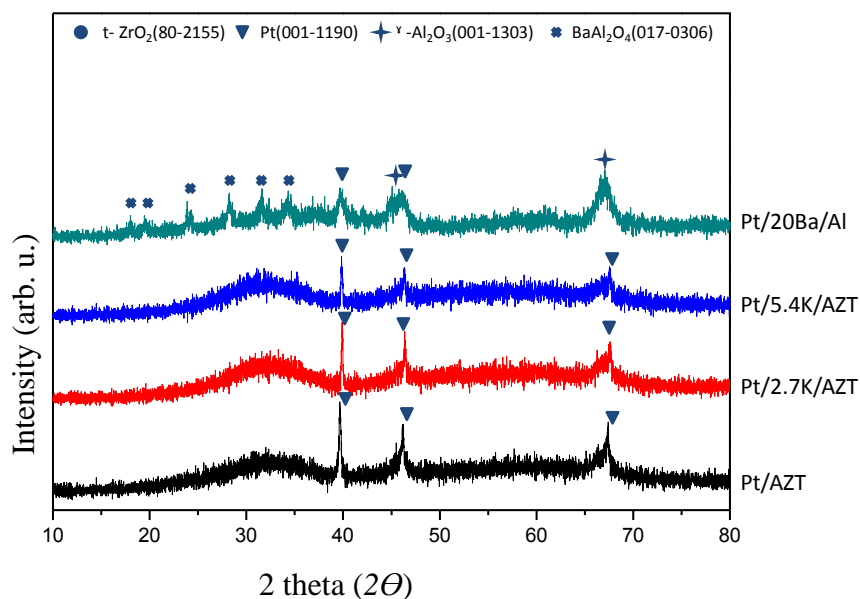


Figure 6 : XRD patterns of the Pt/AZT, Pt/2.7K/AZT, Pt/5.4K/AZT and Pt/20Ba/Al (benchmark) catalysts calcined at 973 K.

For further analysis, the XRD patterns of multi-storage domain materials in the form of Pt/2.7K-8Ba/AZT, Pt/2.7K-20Ba/AZT, Pt/5.4K-8Ba/AZT and Pt/5.4K-20Ba/AZT were investigated (Figure 7). Figure 7 clearly indicates that the intensity of the metallic Pt diffraction features decrease and become broader as compared to the single storage domain materials (Figures 5 and 6). This observation suggests that Pt dispersion could be enhanced in the case of multi-storage domain AZT materials. Furthermore, other minority diffraction signals such as t-ZrO₂ (JCPDS 80-2155) and γ -Al₂O₃ (JCPDS 001-1303) are also visible in Figure 7.

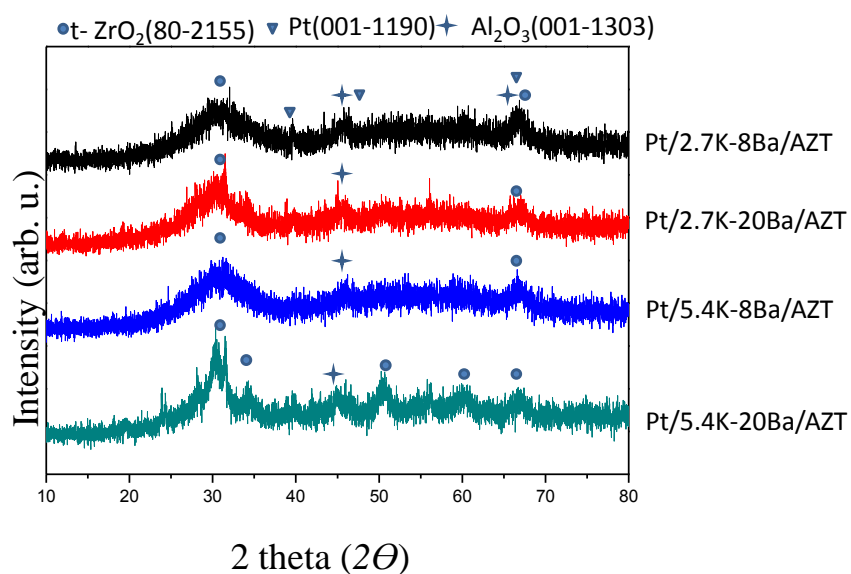


Figure 7 : XRD patterns of the Pt/2.7K-8Ba/AZT, Pt/2.7K-20Ba/AZT, Pt/5.4K-8Ba/AZT and Pt/5.4K-20Ba/AZT catalysts calcined at 973 K.

3.1.2 BET Analysis

Figure 8 represents SSA values of Pt/AZT, Pt/8Ba/AZT, Pt/20Ba/AZT and Pt/20Ba/Al materials. As compared to the benchmark catalysts, Pt/AZT reveals a slightly higher SSA value. Addition of BaO to the Pt/AZT system decreases the SSA monotonically with increasing BaO loading. It should be noted that Pt/20Ba/AZT and Pt/20Ba/Al materials have comparable SSA.

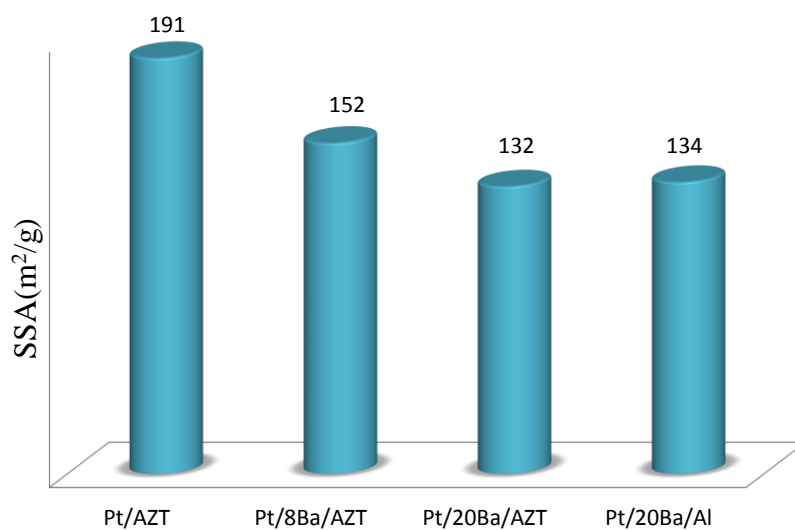


Figure 8 : BET specific surface area values for the Pt/AZT, Pt/8Ba/AZT, Pt/20Ba/AZT catalysts and Pt/20Ba/Al benchmark catalyst after calcination at 973 K.

In Figure 9, SSA values of Pt/AZT, Pt/2.7K/AZT, Pt/5.4K/AZT and Pt/20Ba/Al are presented. It is apparent in Figure 9 that increasing K₂O loading decreases the SSA values of the material where for loadings ≥ 5.4 wt. % K₂O, SSA values tend to converge that of the Pt/20Ba/Al benchmark catalyst.

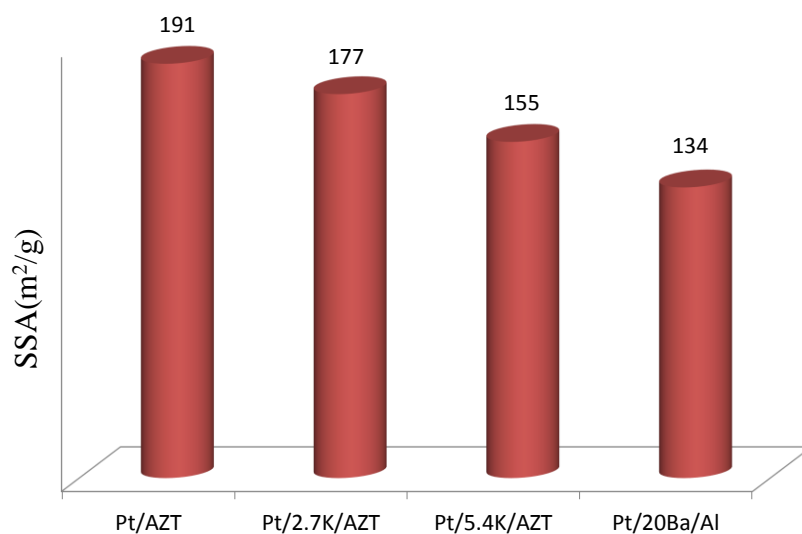


Figure 9 : BET specific surface area values for the Pt/AZT, Pt/2.7K/AZT, Pt/5.4K/AZT catalysts and Pt/20Ba/Al benchmark catalyst after calcination at 973 K.

After having investigated the SSA of single storage domain materials, similar analysis were also performed on multi-storage domain systems. Figure 10 demonstrates the SSA data for Pt/2.7K-8Ba/AZT, Pt/2.7K-20Ba/AZT, Pt/5.4K-8Ba/AZT and Pt/5.4K-20Ba/AZT. In accordance with the aforementioned observations for the single storage domain materials, increasing the loading of the basic oxides (*i.e.* BaO or K₂O) in the multi-storage domain materials also leads to an attenuation in the SSA. While this corresponding decline in SSA is relatively less sensitive to the variations in K₂O loading, it is significantly more prone to alterations in BaO loading (Figure 10).

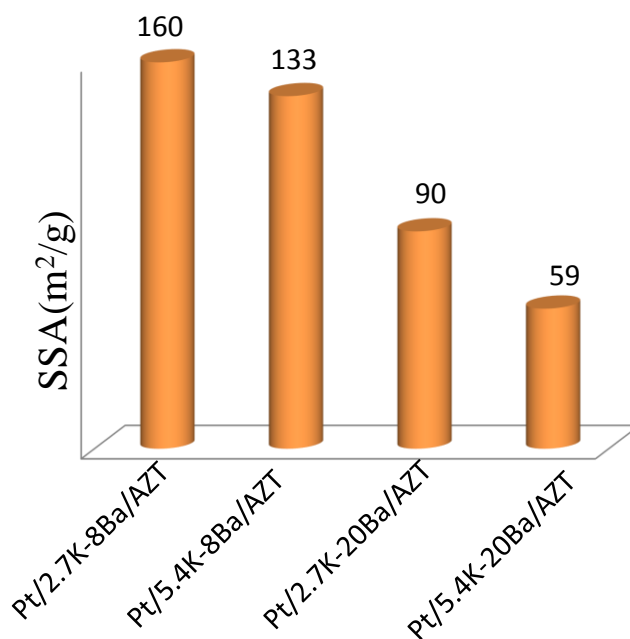


Figure 10 : BET specific surface area values for the K₂O –BaO co-impregnated Pt/2.7K-8Ba/AZT, Pt/2.7K-20Ba/AZT, Pt/5.4K-8Ba/AZT and Pt/5.4K-20Ba/AZT catalysts after calcination at 973K.

3.2 In situ FTIR Analysis

3.2.1 NO_x Adsorption Analysis

3.2.1.1 NO_x Adsorption Analysis of Single Storage Domain Materials

FTIR spectra obtained after NO₂ (g) adsorption (successive 0.5 Torr NO₂ (g) exposure steps with a final saturation exposure of 5 Torr for 10 min) on Pt/AZT sample and its BaO functionalized counterparts at 323 K are illustrated in Figure 11. Five vibrational features were detected, which are located at 1238, 1283, 1561, 1582 and 1640 cm⁻¹ as shown in Figure 11. While vibrational frequencies at 1238

and 1640 cm^{-1} were assigned to bridging nitrates, features located at 1283 , 1582 and 1561 cm^{-1} can be attributed to bidentate nitrates [35, 55]. On the other hand, FTIR spectra of BaO and platinum incorporated AZT samples shown in Figure 11b-c have a different spectral line shape as compared to the Pt/AZT support. In addition to the surface nitrate and nitrite species, bulk/ ionic like nitrate features coordinated to BaO domains are present with characteristic IR frequencies at 1323 , 1452 and 1487 cm^{-1} [35, 56]. It is also clear that abundance of bulk like nitrate species are relatively more pronounced at higher BaO loadings.

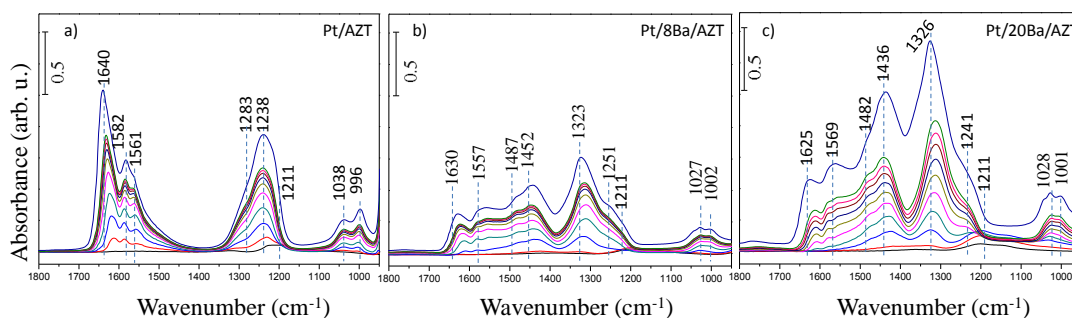


Figure 11 : *In-situ* FTIR spectra of stepwise NO_2 (g) adsorption on activated a) Pt/AZT, b) Pt/8Ba/AZT and c) Pt/20Ba/AZT at 323 K. The topmost spectrum belongs to the saturated surfaces.

In addition to BaO functionalized materials, we further investigated the effect of K_2O loading on the nature of the nitrate coordination chemistry. Thus, stepwise NO_2 (g) adsorption on Pt/AZT, Pt/2.7K/AZT and Pt/5.4K/AZT were monitored as a function of pressure at 323 K as illustrated in Figures 12a-12c, respectively. It should be noted that the molar amount of 2.7 and 5.4 wt. % K_2O were comparable to that of 8 and 20 wt. % BaO in AZT supported materials [57].

IR signals located at 1306 and 1513 cm^{-1} in Figure 12 can be attributed to monodentate nitrates, while the features at 1607 and 1579 cm^{-1} can be assigned to bridging and bidentate nitrates, respectively. In addition to surface nitrates, other features located at 1367 and 1393 cm^{-1} can be assigned to ionic/bulk like potassium nitrates [58, 59]. However, the position of surface and bulk nitrate features are different as compared to that of BaO functionalized counterparts as observed in Figure 11. These complementary results clearly point out to the fact that nitrate coordination is rather sensitive to the metal coordination center.

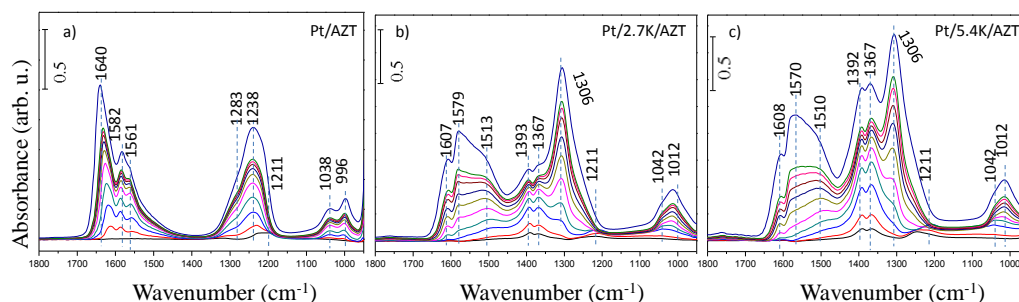


Figure 12 : *In-situ* FTIR spectra of stepwise NO_2 (g) adsorption on activated a) Pt/AZT, b) Pt/2.7K/AZT and c) Pt/5.4K/AZT at 323 K. The topmost spectrum belongs to saturated surface.

3.2.1.2 NO_x Adsorption Analysis of Multi Storage Domain Materials

BaO is the most commonly utilized storage component used in NSR technology [22, 35, 60]. However, its storage ability is well known to be limited at elevated temperatures. Accordingly K_2O has been considered as an alternative storage component and promoter in NSR materials that can boost and widen the

operational temperature window towards higher temperatures [39, 61]. In this section, changes in the NO_x adsorption properties upon simultaneous incorporation of BaO and K₂O on the Pt/AZT system was investigated.

In Figure 13a and 13b, Pt/AZT and Pt/8Ba/AZT samples were used once again as benchmark catalyst in order to be able to compare them with K₂O including counterparts given in Figures 13c and 13d corresponding to Pt/2.7K-8Ba/AZT and Pt/5.4K-8Ba/AZT; respectively. In Figure 13c, there exist six main vibrational features located at 1311, 1352, 1410, 1510, 1580 and 1610 cm⁻¹ on Pt/2.7K-8Ba/AZT. Among these stretchings, 1311 and 1510 cm⁻¹ can be assigned to monodentate nitrates. 1610 and 1580 cm⁻¹ features are associated with the bridging and bidentate nitrates, respectively. Another set of features at 1352 and 1410 cm⁻¹ correspond to bulk like potassium nitrate on BaO domains [59]. In Figures 13c and 13d, although types of surface nitrates and bulk nitrates are rather similar to that of Figures 13a and 13b; their relative intensities change as a function of K₂O loading. As the K₂O loading increases from 2.7 to 5.4 w.t. %, relative IR intensities of bulk like nitrate species (*i.e.* 1393 and 1365 cm⁻¹) on K₂O domains significantly increase. This result points to the fact that K₂O domains are more exposed on the surface of Pt/5.4K-8Ba/AZT while these features are relatively suppressed by BaO domains on the Pt/2.7K-8Ba/AZT catalyst. This observation emphasizes the fact that the surface chemistry of such catalytic systems can be fine-tuned by tailoring surface composition.

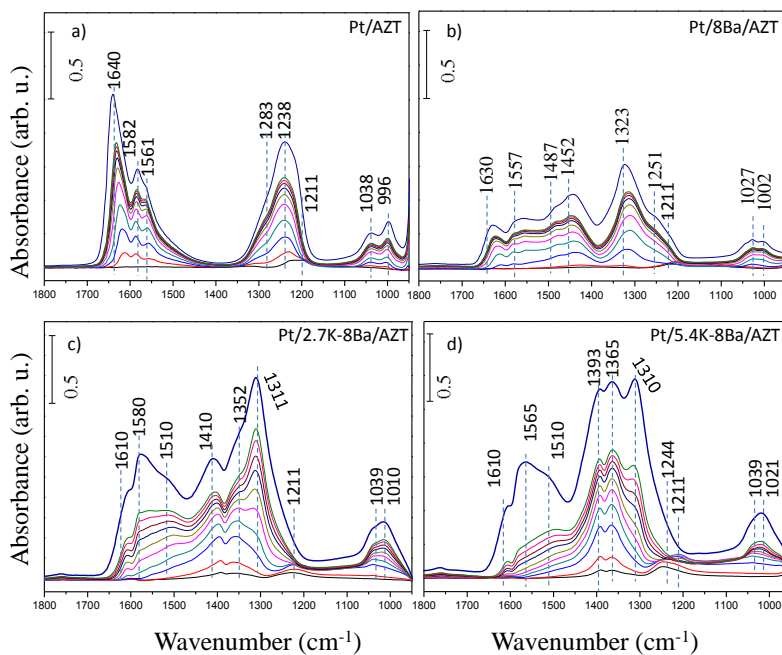


Figure 13 : *In-situ* FTIR spectra of stepwise NO₂ (g) adsorption on activated a) Pt/AZT, b) Pt/8Ba/AZT, c) Pt/2.7K-8Ba/AZT and d) Pt/5.4K-8Ba/AZT at 323 K. The topmost spectrum belongs to saturated surface.

An analogous set of experiments were performed by utilizing 20 wt. % BaO loaded AZT samples co-loaded with different K₂O amounts. In Figure 14, such measurements corresponding to Pt/AZT, Pt/20Ba/AZT, Pt/2.7K-20Ba/AZT and Pt/5.4K-20Ba/AZT are presented. As discussed for the Figure 11, excess BaO loaded sample leads to an increase in the formation of bulk nitrate (1329, 1436 and 1482 cm⁻¹). This trend is also observed in the co-loaded case of K₂O and BaO, where increase in the bulk potassium nitrate suppresses the formation of surface nitrate features [51, 62]. In Figure 14d, there were seven major vibrational features located at 1241, 1312, 1361, 1397, 1510, 1560 and 1610 cm⁻¹. Among these features, 1241 and 1560 cm⁻¹ correspond to bridging nitrates and 1312-1510 cm⁻¹ can be assigned to monodentate nitrates. The other surface nitrate on Pt/5.4K-

20Ba/AZT sample is assigned as a bidentate nitrate that is located at 1610 cm^{-1} [51, 62]. Bulk potassium nitrates are located at 1361 and 1397 cm^{-1} [40, 58, 63].

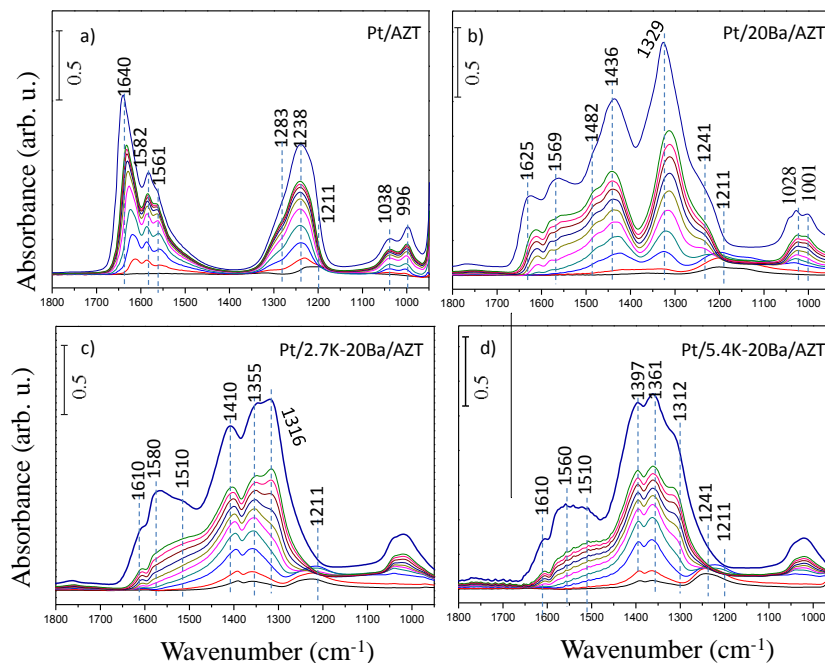


Figure 14 : *In-situ* FTIR spectra of stepwise NO_2 (g) adsorption on activated a) Pt/AZT, b) Pt/20Ba/AZT, c) Pt/2.7K-20Ba/AZT and d) Pt/5.4K-20Ba/AZT at 323 K. The topmost spectrum belongs to saturated surface.

3.2.2 NO_x Reduction Analysis

As well as NO_x adsorption analysis, NO_x reduction over all of the synthesized samples were also performed by using H_2 (g) as the reducing agent to investigate the stability of the surface and bulk nitrate species. First part of such experiments illustrate the initial nitrate reduction of the samples as a function of time. For this purpose, NO_x saturated surface were treated with 15 Torr H_2 (g) at 323K for 40 min (Figure 15, top section). The second part of these experiments are represented in

the middle section of Figure 15 and corresponds to the reduction of the species within the second time interval (60-120 min). The third part is shown in the bottommost section of Figure 15 and is associated with the reduction of the NO_x-saturated surfaces at 373, 473 and 573 K.

3.2.2.1 NO_x Reduction Analysis of Single Storage Domain Materials

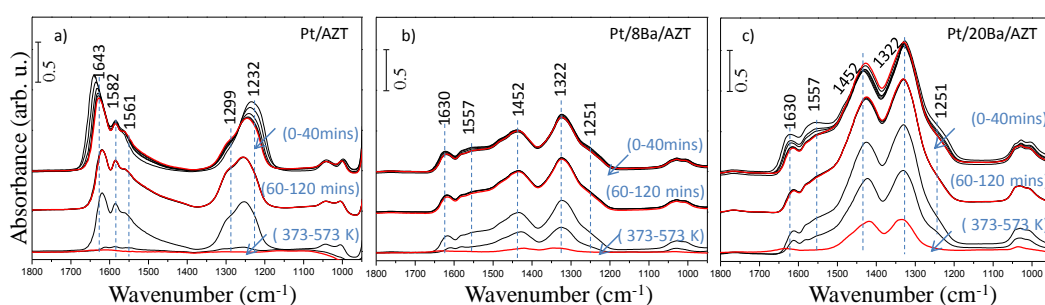


Figure 15 : *In-situ* FTIR spectra of NO₂ (g) reduction *via* H₂(g) on a) Pt/AZT, b) Pt/8Ba/AZT and c) Pt/20Ba/AZT.

In Figure 15a, the set of spectra collected in the first 40 min reveals bridging nitrate features (1643 and 1232 cm⁻¹) on Pt/AZT whose IR intensities decrease after H₂ (g) exposure. This decrease was followed by the formation of monodentate (1299 cm⁻¹) nitrates on the surface. A direct transformation of bridging to monodentate nitrate can be explained by the presence of an isosbestic point at *ca.* 1299 cm⁻¹ in Figure 15a. NO significant spectral changes were observed within the time interval between 60-120 min of H₂ (g) exposure. In the bottommost part of Figure 15a, which is related to the temperature-dependent reduction, surface and bulk nitrates were removed completely at 473 K suggesting full NO_x regeneration

at 473 K in the presence of H_2 (g). A simplified reduction mechanism of nitrate/nitrite functional groups is given in Figure 16.

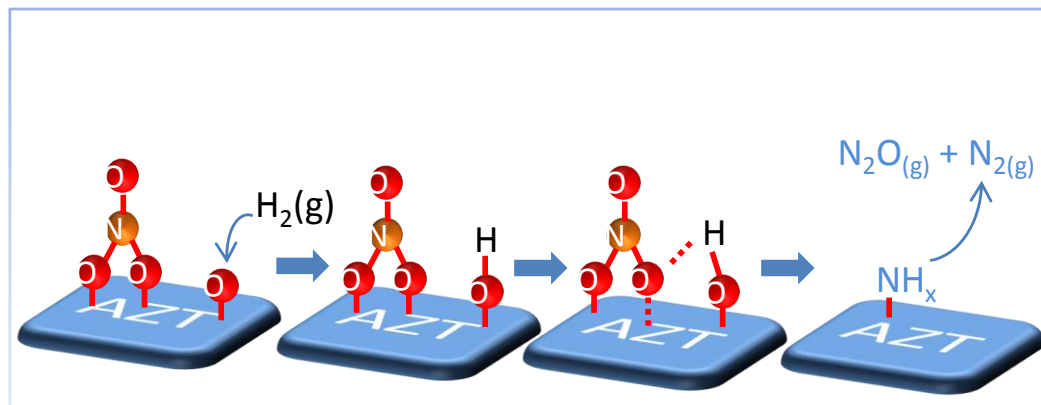


Figure 16 : Schematic representation of nitrate reduction mechanism. (Copyright © 2014 Elsevier. Reproduced with permission from ref [68]).

In Figure 15b and 15c, the reduction of nitrate/nitrite functional groups on Pt/8Ba/AZT and Pt/20Ba/AZT are illustrated. At the end of the time dependent reduction process (*i.e.* after 120 min of H_2 exposure), surface nitrates were relatively decreased, but intensity of the bulk nitrates did not significantly change. On the other hand, during the reduction at elevated temperatures within 373-573 K, intensities of nitrate and nitrite species on Ba loaded samples were gradually decreased. After annealing at 573 K, while Pt/8Ba/AZT sample could be fully regenerated, Pt/20Ba/AZT sample was not completely regenerated. This behavior can be explained by the existence of a large coverage of stable bulk nitrates on the surface of the Pt/20Ba/AZT catalyst which are more resilient towards reduction, as compared to the surface nitrate species that are predominantly present on the Pt/8Ba/AZT surface.

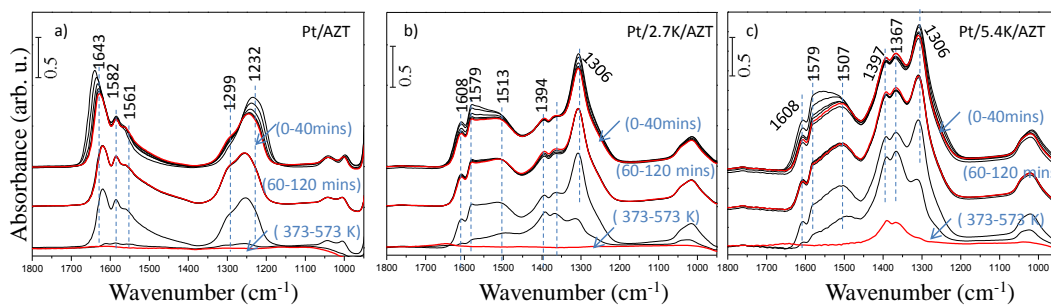


Figure 17 : *In-situ* FTIR spectra of NO₂ (g) reduction via H₂ (g) on a) Pt/AZT, b) Pt/2.7K/AZT and c) Pt/5.4K/AZT.

An identical set of experiments were also performed for the K₂O and Pt incorporated samples. In Figure 17, the reduction behaviors of Pt/AZT, Pt/2.7K/AZT and Pt/5.4K/AZT are shown. In Figure 17b, the absorbance intensity of the surface nitrates slightly decreases in the presence of 15 Torr H₂ (g) in the first 40 min of the reduction process at 323 K. After this initial period, further reduction of surface and bulk nitrate features were not observed. During the temperature-dependent reduction experiments, regeneration of the Pt/2.7K/AZT was fully accomplished at 573 K; however, Pt/5.4K/AZT sample could not be completely regenerated at 573 K due to the presence of an extensive amount of bulk nitrates on the latter surface.

3.2.2.2 NO_x Reduction Analysis of Multi Storage Domain Materials

Similar NO_x reduction experiments were also performed over multi storage domain containing AZT-based catalysts. Figure 18 shows the corresponding *in-situ* FTIR spectra for the Pt/AZT, Pt/8Ba/AZT, Pt/2.7K-8Ba/AZT and Pt/5.4K-

8Ba/AZT samples, where the first two samples are shown for comparison. H₂ (g) exposure on the Pt/2.7K-8Ba/AZT and Pt/5.4K-8Ba/AZT sample surfaces at 323 K in the first 40 min (Figure 18c and 18d), leads to the partial removal of monodentate (1311, 1510 cm⁻¹), bridging (1580 cm⁻¹) and bidentate nitrates (1610 cm⁻¹). In the second time interval (*i.e.* within 60-120 min of H₂ (g) exposure), bulk potassium nitrates (1352 and 1410 cm⁻¹) start to attenuate in a minor fashion. Figures 18c and 18d indicate that at elevated temperature reduction, the surface nitrate functional groups are decomposed first, followed by the reduction of the bulk nitrates. Furthermore, the monodentate surface nitrates were found to be more stable than the other surface nitrate species. Experimental findings, given in Figures 15, 17 and 18 can be analyzed comparatively in order to understand the relative NO_x reduction capabilities of single storage domain AZT catalysts (*i.e.* Pt/8Ba/AZT and Pt/2.7 or 5.4 K/AZT; respectively) and their multi-storage domain counterparts at low BaO coverages (*i.e.* Pt/2.7K-8Ba/AZT and Pt/5.4K-8Ba/AZT). It can be seen that NO_x reduction capabilities of Pt/8Ba/AZT (Figure 15b) and Pt/2.7K/AZT (Figure 17b) are rather comparable, where both of these catalysts can be fully regenerated at 573 K. In contrast, increasing the K₂O loading to 5.4 wt.% leads to the formation of a large amount of bulk KNO₃ species (see Figure 17c for Pt/5.4K/AZT) where a relatively larger portion of bulk nitrates stay intact even after reduction at 573 K. On the other hand, comparison of the reduction data given in Figures 17c, 18b and 18 d for Pt/5.4K/AZT, Pt/8Ba/AZT and Pt/5.4K-8Ba/AZT; respectively suggest that, by utilizing multi-storage domains, one can fine-tune the stability of the bulk nitrates generated on the catalyst surface under reducing conditions at 573 K, where Pt/5.4K-8Ba/AZT (Figure 18d) reveals bulk nitrates which are more resilient

towards reduction than that of Pt/8Ba/AZT (Figure 18b) but are easier to be reduced than that of Pt/5.4K/AZT (Figure 17c) [12, 64-66].

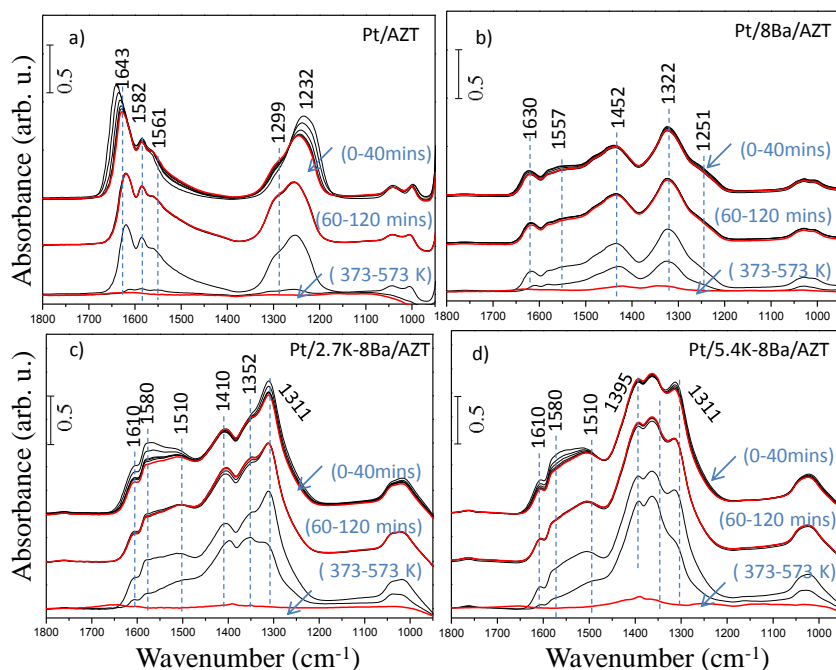


Figure 18 : *In-situ* FTIR spectra of NO₂ (g) reduction *via* H₂ (g) on saturated a) Pt/AZT, b) Pt/8Ba/AZT, c) Pt/2.7K-8Ba/AZT and d) Pt/5.4K-8Ba/AZT.

Figure 19 demonstrates the changes in the surface functional groups on Pt/AZT, Pt/20Ba/AZT, Pt/2.7K-20Ba/AZT and Pt/5.4K-20Ba/AZT samples containing a higher loading of BaO during the NO_x reduction process performed under identical experimental conditions, described above. It is clear that increasing the storage domain loading in single storage domain materials increases the stability of the stored nitrates towards reduction (*e.g.* compare Figures 15b vs 15c for Pt/8Ba/AZT and Pt/20Ba/AZT or Figures 17b and 17c for Pt/2.7K/AZT and Pt/5.4K/AZT, respectively). On the other hand, comparing this result with that of Figure 19d for the Pt/5.4K-20Ba/AZT sample reveals that even in the co-presence

of high loadings of BaO and K₂O, the reduction resistance of the catalyst lies in between Pt/20Ba/AZT and Pt/5.4K/AZT. This important finding suggest that as in the case of low BaO loadings, stability of the surface nitrates can also be fine-tuned at higher BaO loadings by using K₂O as a complementary storage domain. [67, 68]

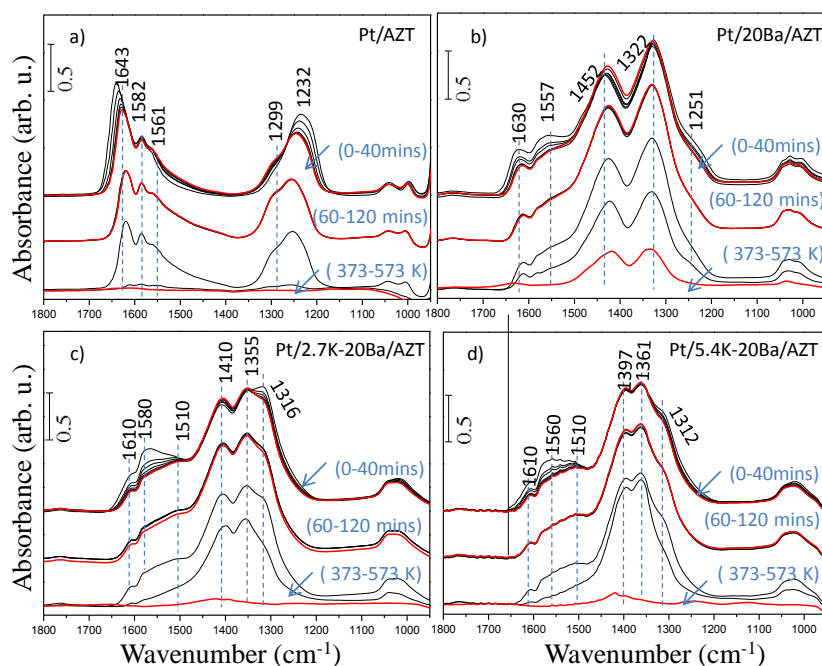


Figure 19 : *In-situ* FTIR spectra of NO₂ (g) reduction *via* H₂ (g) on saturated a) Pt/AZT, b) Pt/20Ba/AZT, c) Pt/2.7K-20Ba/AZT and d) Pt/5.4.K-20Ba/AZT.

3.2.3 SO_x Adsorption Analysis

In this section, SO_x uptake capacity and adsorption characteristics of the single and multi-storage domain AZT catalysts are investigated as a function of temperature *via in-situ* FTIR spectroscopy.

3.2.3.1 SO_x Adsorption Analysis of Single Storage Domain Materials

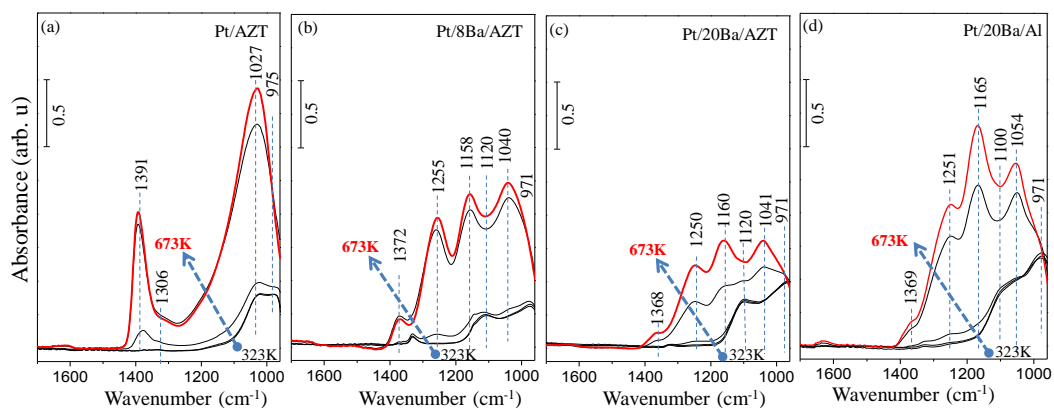


Figure 20 : *In-situ* FTIR spectra related to the SO_x uptake properties of a) Pt/AZT, b) Pt/8Ba/AZT, c) Pt/20Ba/AZT and d) Pt/20Ba/Al that are exposed to 2 Torr SO_x at 323 K, followed by annealing at 373, 473, 573 and 673 K in the presence of the SO_x gas mixture for 5 min.

Figure 20 represents temperature dependent sulfur poisoning experiments on the surfaces of Pt/AZT, Pt/8Ba/AZT and Pt/20Ba/AZT and the Pt/20Ba/Al benchmark catalyst under 2 Torr SO_x exposure at 323 K and followed by annealing at higher temperatures in the presence of the SO_x gas mixture. In Figure 20a, four major vibrational features at 1391, 1306, 1027 and 975 cm⁻¹ were observed. Two of these, 1027 and 975 cm⁻¹ features, which were the major signals at low temperature experiments, can be assigned to sulfate (SO₄²⁻) and sulfite (SO₃²⁻) species, respectively [69, 70]. Other vibrational features, 1391 and 1306 cm⁻¹ can be attributed to bidentate and tridentate surface sulfate species, respectively. When the temperature was increased in the SO_x gas mixture, absorbance of the sulfate/sulfite functional groups increased [71, 72]. Figure 20b and 20c correspond

to Pt/8Ba/AZT and Pt/20Ba/AZT, respectively. BaO loaded AZT samples and benchmark catalyst (Pt/20Ba/Al) reveal significantly different spectral line shapes as compared to the Pt/AZT sample; where at low temperatures (323 K and 373 K), two major features at 1120 and 971 cm^{-1} are visible, which can be assigned to surface sulfate and sulfite species [73]. At higher temperatures new vibrational features at 1370, 1250, 1165 and 1054 cm^{-1} appear. Two of these features located at 1250 and 1054 cm^{-1} can be assigned to bulk-like sulfates on BaO domains, while other vibrational features at 1165 and 1370 cm^{-1} can be attributed to surface sulfates on catalysts surfaces [71, 73-75].

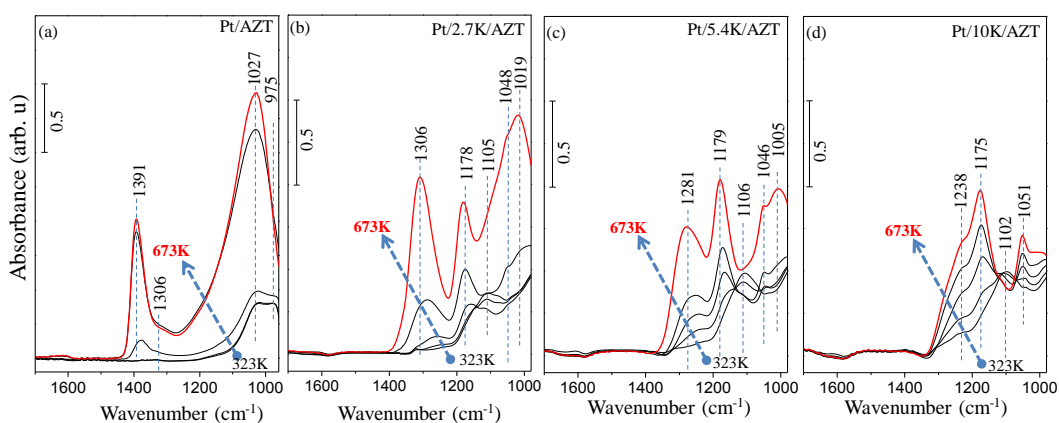


Figure 21 : *In-situ* FTIR spectra related to the SO_x uptake properties of a) Pt/AZT, b)Pt/2.7K/AZT, c)Pt/5.4K/AZT and d) Pt/10K/AZT exposed to 2 Torr SO_x at 323 K, followed by annealing at 373, 473, 573 and 673 K in the presence of SO_x gas mixture for 5 min (Copyright © 2016 Elsevier. Reproduced with permission from ref [49]).

Similar set of experiments were also performed for K_2O loaded AZT samples. In Figure 21, sulfur poisoning of Pt/AZT, Pt/2.7K/AZT, Pt/5.4K/AZT and

Pt/10K/AZT samples are shown. In Figure 21b (corresponding to the sulfur uptake experiments on Pt/2.7K/AZT), five vibrational features at 1306, 1178, 1105, 1048 and 1019 cm^{-1} were observed. The features at 1178 and 1048 cm^{-1} can be attributed to bulk-like sulfate on basic storage domain (K_2O) [73, 76]. The rest of the vibrational features can be assigned to surface sulfate functional groups on the AZT support. Figures 21c and 21d represent sulfur poisoning experiments on the Pt/5.4K/AZT and Pt/10K/AZT samples, respectively. Both of the FTIR spectra yield similar surface sulfate groups where the most prominent feature was at 1178 cm^{-1} that can be ascribed to bulk-like sulfates on K_2O . For the Pt/5.4K/AZT and Pt/10K/AZT samples, lack of 1391 and 1306 cm^{-1} features which are associated to the surface sulfate species on AZT sample indicates that at high K_2O loadings, most of the surface of the AZT support is covered by the K_2O domains. Along these lines, other vibrational features (1306, 1105, 1048 and 1019 cm^{-1}) can be assigned to surface sulfate species on K_2O domains (Figures 21c and 21d) [72-74, 76].

Kim *et al.* reported that an increase in K_2O loading increases the NO_x storage capacity of the sample within 600-800 K [62]. On the other hand, as seen in Figure 21d, excess K_2O loadings on AZT surface cause extensive sulfur poisoning. Thus, we decided to utilize low (2.7K) or moderate (5.4K) K_2O loading samples in the forthcoming analogous sulfur poisoning experiments on multi-storage domain catalysts.

3.2.3.2 SO_x Adsorption Analysis of Multi Storage Domain Materials

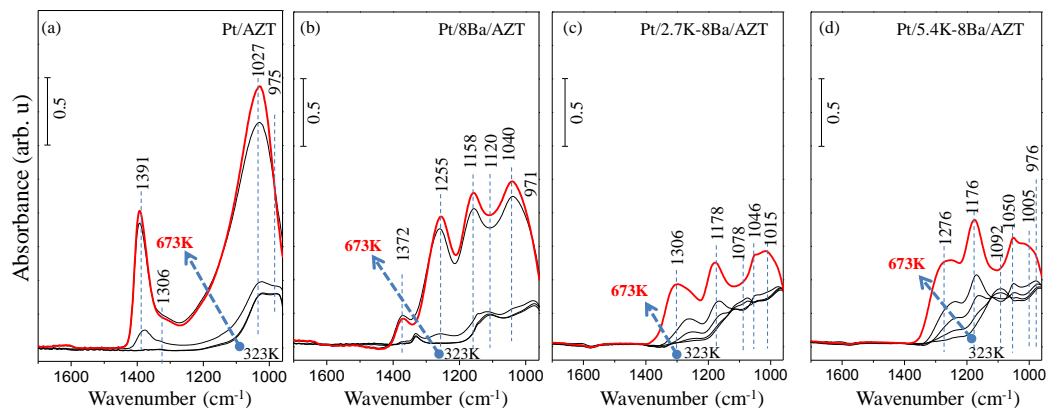


Figure 22 : *In-situ* FTIR spectra related to SO_x uptake properties of a) Pt/AZT, b) Pt/8Ba/AZT, c) Pt/2.7K-8Ba/AZT and d) Pt/5.4K-8Ba/AZT exposed to 2 Torr SO_x at 323 K, followed by annealing at 373, 473, 573 and 673 K in the presence of SO_x gas mixture for 5 min.

In Figure 22, the sulfur poisoning experiments of Pt/AZT, Pt/8Ba/AZT, Pt/2.7K-8Ba/AZT and Pt/5.4K-8Ba/AZT are depicted. Relevant data for Pt/AZT and Pt/8Ba/AZT are also given for comparison. In Figures 22c and 22d, at low temperatures, the major vibrational features appear at 1092/1078 and 976 cm⁻¹ that correspond to surface sulfates and sulfites, respectively. At high temperatures, the surface sulfate species (1306, 1078, 1046 and 1015) grow in intensity suggesting the thermal oxidation of sulfite species to sulfates [71, 75].

As mentioned above, the 1176 cm⁻¹ feature can be assigned to bulk like sulfates on K₂O domains. A comparative analysis of Figures 20, 21 and 22 reveals that, for the single storage domain materials, increasing the loading of the basic

storage domain (BaO or K₂O) increases the sulfur uptake under oxidizing conditions particularly at elevated temperatures (e.g. 673 K). On the other hand for low BaO loadings (i.e. 8wt. %, Figure 22b), incorporation of 2.7 or 5.4wt. % K₂O (Figures 22c and 22d) to obtain multi-storage domain materials leads to an attenuation of the sulfur uptake.

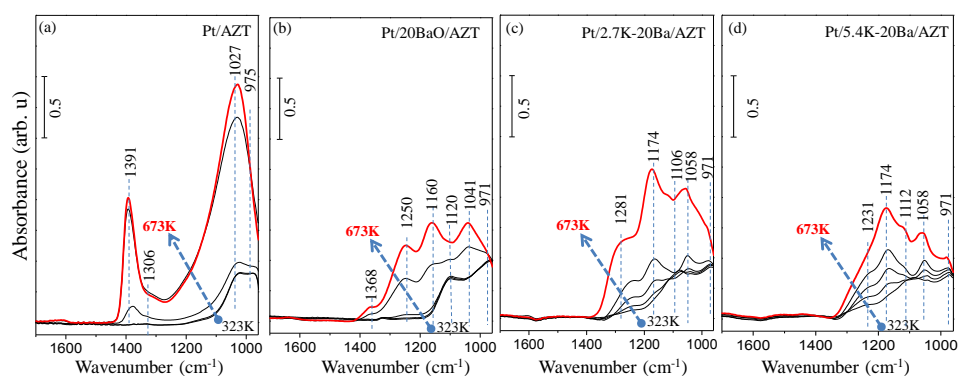


Figure 23 : *In-situ* FTIR spectra related to SO_x uptake properties of a) Pt/AZT, b) Pt/20Ba/AZT, c) Pt/2.7K-20Ba/AZT and d) Pt/5.4K-20Ba/AZT that exposed to 2 Torr SO_x at 323 K, followed by annealing at 373, 473, 573 and 673 K in the presence of SO_x gas mixture for 5 min.

Excess BaO and low and moderate K₂O co-loaded samples were also utilized in analogous sulfur poisoning experiments. In Figure 23, such experimental results for Pt/AZT, Pt/20Ba/AZT Pt/2.7K-20Ba/AZT and Pt/5.4K-20Ba/AZT are given. Unlike the results given in Figure 22, Figure 23 suggests that for the high BaO loading of 20 wt.%, incorporation of additional K₂O domains increase the sulfur uptake. This may indicate that 20wt.% BaO loading with additional K₂O domains may lead to an extremely basic surface making the catalyst awfully susceptible for sulfur poisoning. In addition it should be noted that, vibrational features located at

1280 and 1250 cm^{-1} which were assigned to bulk-like sulfates on BaO domains, did not exist on the surface of Pt/5.4K-20Ba/AZT sample, indicating that K_2O domains may be covering most of the BaO domains on this catalyst.

3.2.4 SO_x Reduction Analysis

The sulfur regeneration of the samples is crucial for the long lasting NO_x uptake capacity of the NSR catalysts. Thus in order to shed light on sulfur regeneration abilities, after the sulfur poisoning experiments, the samples were also exposed to 15 Torr external reducing agent (H_2 (g)) at 323 K and heating in H_2 (g) at 473, 673, 773, 873 and 973 K to remove S-related species.

3.2.4.1 SO_x Reduction Analysis of Single Storage Domain Materials

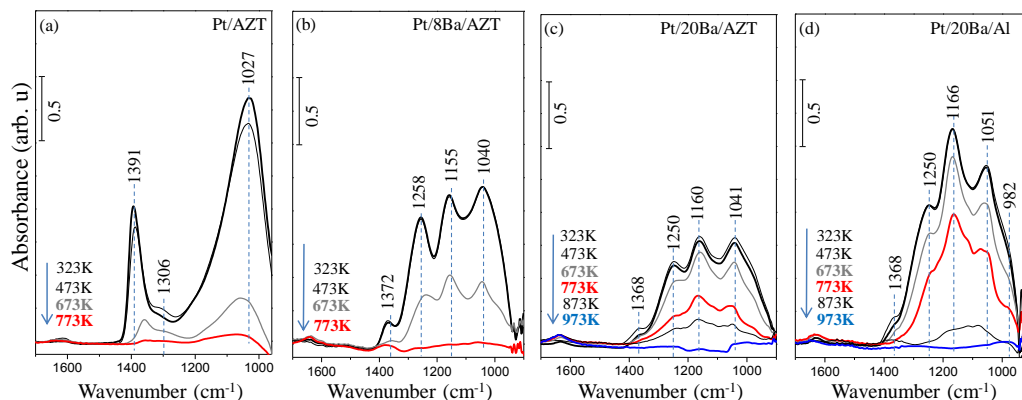


Figure 24 : *In-situ* FTIR spectra related to SO_x reduction properties of a) Pt/AZT, b) Pt/8Ba/AZT, c) Pt/20Ba/AZT and d) Pt/20Ba/Al samples via H₂ (g). The catalysts were initially poisoned by 2 Torr SO_x. After evacuation, poisoned samples were exposed to 15 Torr H₂ (g) at 323, 473, 673 and 773 K for 5 min. All spectra were acquired at 323 K.

Figure 24 presents the SO_x regeneration characteristics of the Pt/AZT, Pt/8Ba/AZT, Pt/20Ba/AZT and Pt/20Ba/Al under reducing conditions as a function of temperature. In Figure 24a, at relatively low temperatures (323,473K) H₂ (g) exposure did not significantly change the vibrational features on the surface of Pt/AZT however it could be fully regenerated from sulfur at 773 K. As shown in Figures 24b and 24c, while low BaO loading sample was completely regenerated at 773 K, high BaO loading sample was not fully regenerated below 973 K. The Pt/20Ba/Al benchmark catalyst shown in Figure 24d also suffers from sulfur poisoning and its regeneration also requires a high temperature ($T \geq 973$ K).

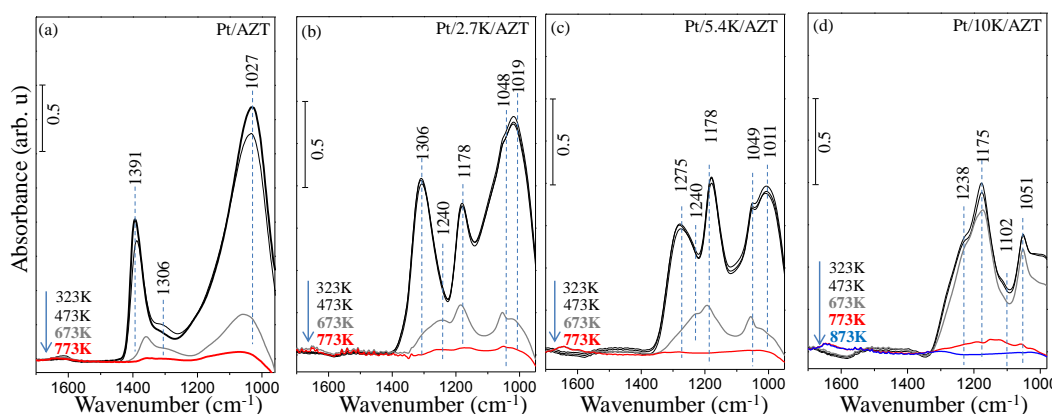


Figure 25 : *In-situ* FTIR spectra related to SO_x reduction properties of a) Pt/AZT, b)Pt/2.7K/AZT, c)Pt/5.4K/AZT and d) Pt/10K/AZT samples via H₂ (g). The poisoned samples were exposed to 15 Torr H₂ (g) at 323, 473, 673, 773 and 873 K for 5 min. All spectra were acquired at 323 K (Copyright © 2016 Elsevier. Reproduced with permission from ref. Copyright 2016 Elsevier B.V. [49].

Identical series of experiments were illustrated for K₂O based AZT samples in Figure 25. As shown in Figure 25, the spectral line shapes of these samples did not change significantly up to annealing at 473 K. In contrast, increasing the reduction temperature to 773 K led to the complete reduction of SO_x species on Pt/AZT, Pt/2.7K/AZT, and Pt/5.4K/AZT (Figures 25a-25c) while a minor SO_x residue still remained on the Pt/10K/AZT. This behavior is in stark contrast to that of the Pt/20Ba/Al benchmark catalyst (Figure 24d) where a significantly greater amount of sulfur-containing functional groups remained on the surface after an identical treatment. Therefore it can be suggested that low and moderate K₂O loadings on the AZT support display superior sulfur removal performance in the presence of a reducing agent than that of the conventional benchmark catalyst [49].

3.2.4.2 SO_x Reduction Analysis of Multi Storage Domain Materials

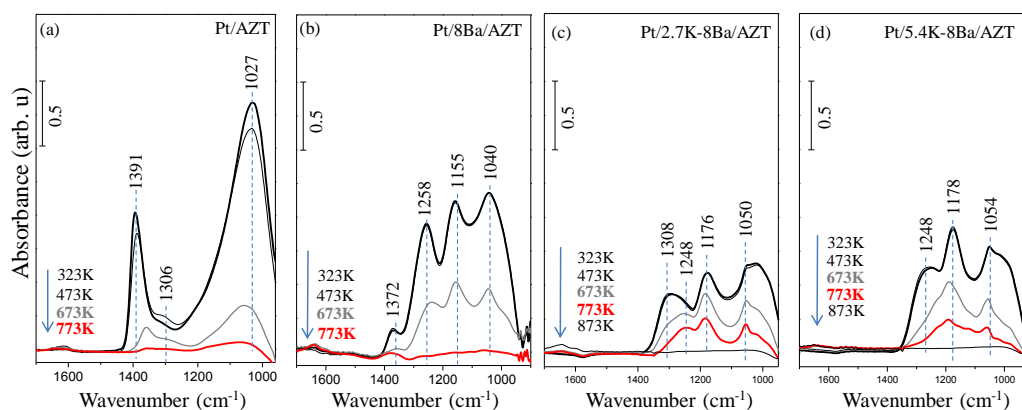


Figure 26 : *In-situ* FTIR spectra related to SO_x reduction properties of a) Pt/AZT, b) Pt/8Ba/AZT c) Pt/2.7K-8Ba/AZT, d) Pt/5.4K-8Ba/AZT and samples via H₂ (g). The poisoned samples were exposed to 15 Torr H₂ (g) at 323, 473, 673, 773 and 873 K for 5 min. All spectra were acquired at 323 K.

Figure 26 illustrates SO_x reduction properties of low BaO loading K₂O co-impregnated samples in comparison to that Pt/AZT and Pt/8Ba/AZT. It can be seen in Figure 26 that complete SO_x reduction via H₂ on Pt/2.7K-8Ba/AZT and Pt/5.4K-8Ba/AZT requires temperatures above 873 K. In other words, sulfite/sulfate species generated on Pt/2.7K-8Ba/AZT and Pt/5.4K-8Ba/AZT samples with low BaO loading are more resilient to reduction than that of their single storage domain counter parts such as Pt/8Ba/AZT (Figure 26b), Pt/2.7K/AZT (Figure 25b) or Pt/5.4K/AZT (Figure 25c). It is important to note that although it could be reasonable to utilize IR intensities to compare relative amounts of adsorbates on

different catalyst surfaces, an exact quantitative comparison should be avoided due to the differences in the IR absorption cross sections of different oscillators located at different adsorption sites [77].

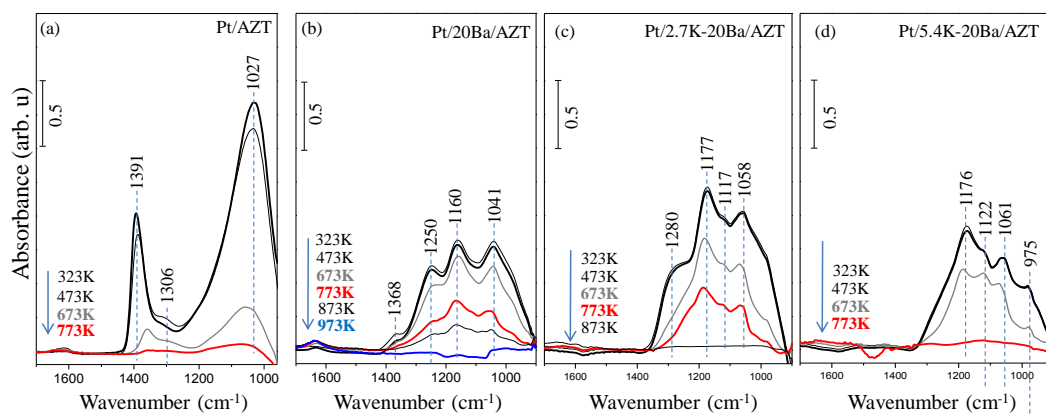


Figure 27 : *In-situ* FTIR spectra related to SO_x reduction properties of a) Pt/AZT, b) Pt/20Ba/AZT c) Pt/2.7K-20Ba/AZT, d) Pt/5.4K-20Ba/AZT and samples via H₂ (g). The poisoned samples were exposed to 15 Torr H₂ (g) at 323, 473, 673, 773 and 873 K for 5 min. All spectra were acquired at 323 K.

In Figure 27, SO_x reduction performances of Pt/AZT and excess baria and low/moderate potassium oxide co-loaded mixed oxides are shown as a function of temperature by means of *in-situ* FTIR spectroscopy. The surface functional groups on the surface of the catalysts with excess baria, co-loaded with K₂O (Pt/2.7K-20Ba/AZT and Pt/5.4K-20Ba/AZT, Figures 27c and 27d) showed similarities to that of Pt/20Ba/AZT sample (Figure 27b). However, vibrational features located at 1280 and 1250 cm⁻¹ which were assigned to bulk-like sulfates on K₂O and BaO domains, respectively did not exist on the surface of Pt/5.4K-20Ba/AZT sample.

The lack of bulk-like sulfates can provide an explanation regarding the sulfur removal capability of Pt/5.4K-20Ba/AZT at a relatively low temperature (773 K).

3.3 TPD Analysis

Temperature programmed desorption analysis was performed in order to gain quantitative insight regarding the total NO_x adsorption capacity and thermal stabilities of adsorbed surface features in vacuum. Before the TPD experiments, samples were saturated by NO_x or SO_x gases. After saturation, the FTIR spectrum was recorded and the system was outgassed at 1×10^{-4} Torr for 40 min. At the end of the TPD experiment, the FTIR spectrum was acquired once again to analyze the residual surface species remaining on the samples.

3.3.1 NO_x TPD Analysis

For the NO_x TPD experiments, samples were saturated with 5 Torr NO₂ (g) at 323 K for 10 min. After the degassing process, samples were heated to 973 K with a heating ramp of 12 K/min. TPD experiment was monitored by recording the QMS signals with the mass to charge ratios (m/z) equal to 28 (N₂), 32(O₂), 30(NO), 44(N₂O), 46(NO₂) and 18 (H₂O).

The quantitative analysis of the integrated TPD spectra was performed by using the corresponding mass spectroscopic fragmentation patterns of the gas phase species [35]. For calculation of the total integrated TPD spectrum of NO₂, NO (m/z = 30) and NO₂ (m/z = 46) channels are considered. NO (m/z = 30) to NO₂ (m/z = 46) intensity ratio of 3.23 was obtained by analysis of pure NO₂ *via* current QMS.

Thus, for calculation of NO₂ TPD signal, intensity of NO₂ (*I* 46) signal is multiplied by a factor of 4.23 (3.23 +1.00).

$$\sum NO_2 = \left(\int I_{46} \Delta T \right) \times 4.23$$

In order to calculate the total integrated TPD signal of N₂O, NO (*m/z* = 30) and N₂O (*m/z* = 44) channels are considered. NO (*m/z* = 30) to N₂O (*m/z* = 44) intensity ratio of 0.34 upon fragmentation pattern in the QMS was considered. Thus, for calculation of N₂O TPD signal, intensity of N₂O (*I* 44) signal is multiplied by a factor of 1.34 (0.34 +1.00).

$$\sum N_2O = \left(\int I_{44} \Delta T \right) \times 1.34$$

For calculation of the total integrated TPD spectrum of N₂, N₂ (*m/z* = 28) channel is considered. However, this channel has also contribution from N₂O (*m/z* = 44). Hence, for calculation of N₂ TPD signal, contribution from N₂O is subtracted from the integrated N₂ signal. Contribution of N₂O (*m/z* = 44) in N₂ signal is 0.11 times the N₂O (*I* 44) signal.

$$\sum N_2 = \left[\left(\int I_{28} \Delta T \right) - \left(\int I_{44} \Delta T \right) \times 0.11 \right]$$

For calculation of the total integrated TPD spectrum of NO, NO (*m/z* = 30) channel is considered. However, this channel has also contribution from N₂O (*m/z* = 44) and NO₂ (*m/z* = 46). Hence, for calculation of the net NO integrated TPD signal, contributions from NO₂ and N₂O are subtracted from the integrated NO (*I*30)

signal. Contribution of NO₂ to NO signal is 3.23 times the m/z=30 signal, while contribution of N₂O to NO signal is 0.34 times the m/z=30 signal.

$$\sum NO = (\int I_{30} \Delta T) - (\int I_{46} \Delta T) \times 3.23 - (\int I_{44} \Delta T) \times 0.34$$

In order to calculate the total number of NO_x molecules adsorbed on the surface, nitrogen mass balance should be considered. Thus, total amount of adsorbed NO_x species can be estimated as follows:

$$\sum NSC = \sum NO_2 + 2x \sum N_2O + 2x \sum N_2 + \sum NO$$

After the calculation of the total integrated area of each desorption channel, the NO_x storage capacity of the catalyst is calculated. Moreover, NO_x storage capacity of each catalyst was normalized by the SSA of the catalyst.

3.3.1.1 NO_x TPD Analysis Single Storage Domain Materials

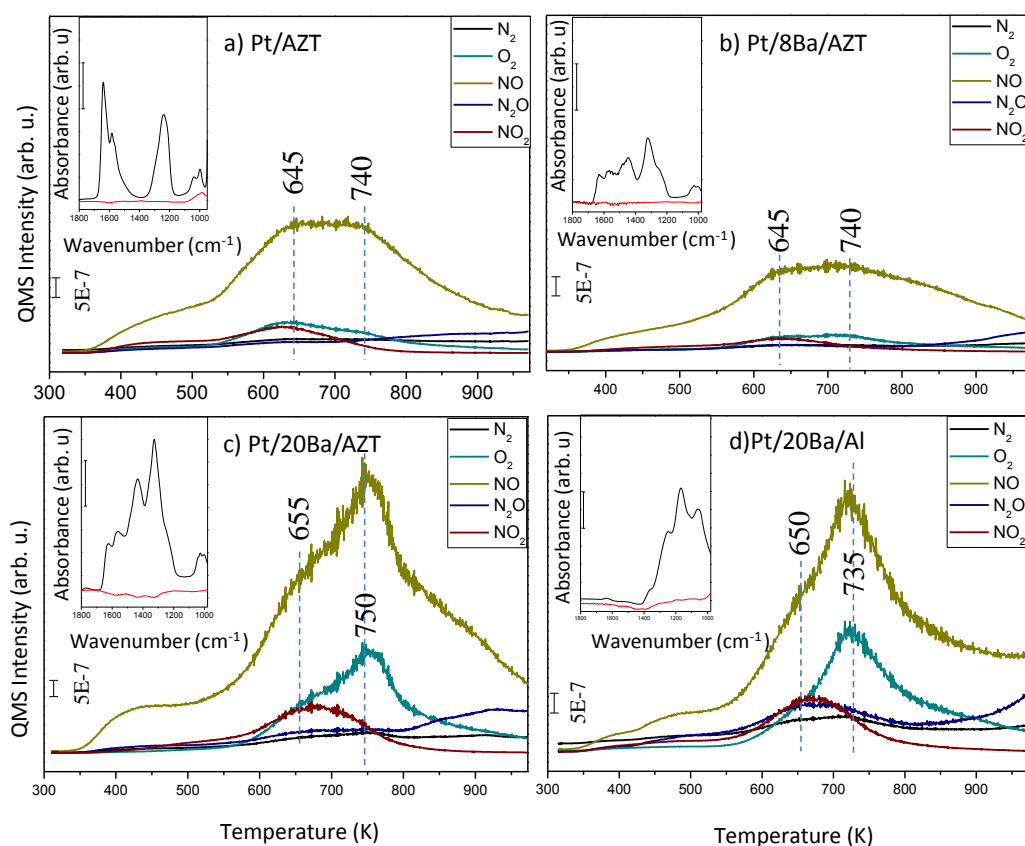
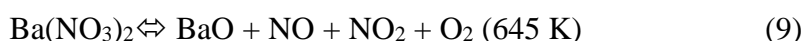


Figure 28 : NO_x TPD profiles for a) Pt/AZT, b) Pt/8Ba/AZT c) Pt/20Ba/AZT, d) Pt/20Ba/Al samples after saturation with 5 Torr NO₂ (g) at 323 K for 10 min. The inset spectra in each panel represent *in-situ* FTIR spectra before (black) and after (red) TPD analysis.

Figure 28 shows TPD profiles corresponding to the thermal decomposition of nitrate and nitrite species on Pt/AZT, Pt/8Ba/AZT, Pt/20Ba/AZT and Pt/20Ba/Al samples. At low temperatures such as 645 K, NO_x decomposition -originating from surface nitrates- was mainly in the form of NO₂ + O₂ (Note that m/z=46:m/z=30 QMS fragmentation ratio for pure NO₂ is about 1:3). On the other hand, at high

temperatures such as 740 K, the NO_x decomposition -due to bulk nitrates- was mostly in the form of NO(g)+O₂(g). In Figures 28c and 28d, NO_x TPD spectra of 20wt.% BaO loaded catalysts are shown. For these catalysts, the major desorption signal appears at elevated temperatures revealing the formation of NO(g) +O₂(g) as the decomposition products. These findings allow us to suggest the following temperature-dependent nitrate decomposition pathways on Pt/Ba/AZT samples:



In order to analyze the thermal regeneration of the samples, *in-situ* FTIR spectra were acquired before (black spectra) and after (red spectra) TPD experiments (see insets in Figure 28). It is clear that all of the adsorbed nitrate/nitrite species on surface of the samples were removed after TPD experiments for all samples.

Surface area normalized NO_x storage capacity (NSC) values of the Pt/AZT, Pt/8Ba/AZT, Pt/20Ba/AZT, and Pt/20Ba/Al catalysts were calculated using the TPD data given in Figure 28 and presented in Figure 29. Figure 29 clearly indicates that increasing the BaO loading on the AZT support monotonically increases the NSC up to 20wt.%. Furthermore, Pt/20Ba/AZT sample exceeds the NSC of the Pt/20Ba/Al benchmark catalyst by ca. 21%.

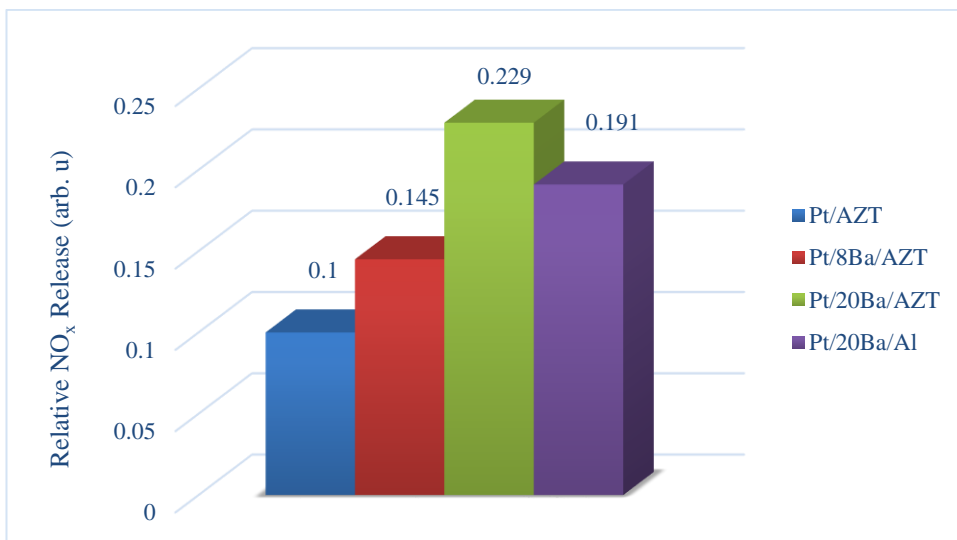


Figure 29 : Surface area normalized NSC values of BaO loaded AZT catalysts obtained from integrated NO_x TPD signals.

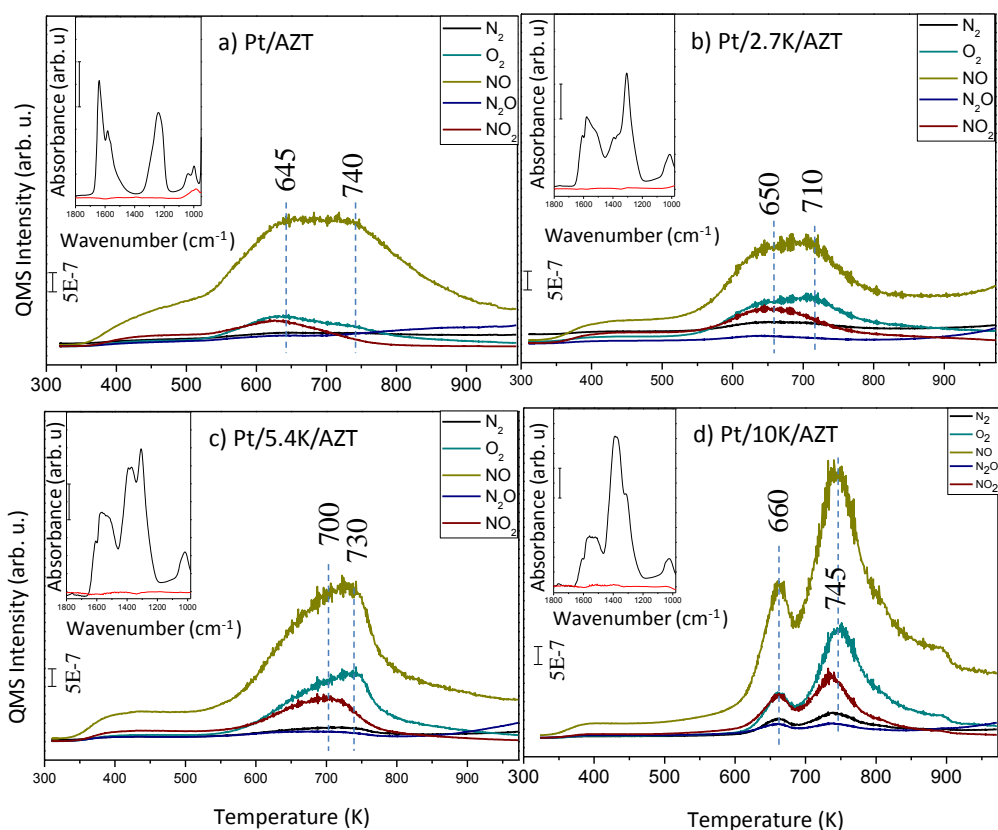
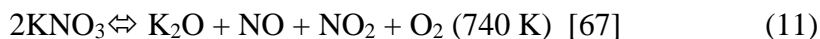


Figure 30 : NO_x TPD profiles for a) Pt/AZT, b) Pt/2.7K/AZT c) Pt/5.4K/AZT, d) Pt/10K/AZT samples after saturation with 5 Torr NO₂ (g) at 323 K for 10 min. The inset spectra in each panel represent *in-situ* FTIR spectra before (black) and after (red) TPD analysis.

Identical set of TPD experiments were also performed for K₂O containing AZT-based catalysts. Corresponding TPD profiles of Pt/AZT, Pt/2.7K/AZT, Pt/5.4K/AZT and Pt/10 K/AZT catalysts are illustrated in Figure 30. TPD spectra of Pt/AZT and Pt/2.7K/AZT reveal similar features (Figures 30a and 30b). It is apparent that the high temperature NO_x desorption in the form of NO + O₂ monotonically increases with increasing K₂O loadings (Figures 30c and 30d) which

is consistent with the increase in the relative amount of bulk nitrates on the catalyst surfaces. Thermal decomposition of such bulk-like can be envisaged as follows:



As can be seen in the insets of Figure 30, all samples can be fully regenerated from NO_x species after the TPD experiments.

SSA normalized NSC values obtained from the integrated NO_x TPD signals of K_2O loaded AZT catalysts are illustrated in Figure 31. SSA normalized NSC values can be ranked as follows: $\text{Pt}/10\text{K}/\text{AZT} > \text{Pt}/5.4\text{K}/\text{AZT} > \text{Pt}/2.7\text{K}/\text{AZT} > \text{Pt}/\text{AZT}$. As expected, increasing K_2O loading monotonically increases the NSC of the samples. It is worth mentioning that the NSC value potassium oxide based AZT catalyst relatively converges to that of $\text{Pt}/20\text{Ba}/\text{Al}$ benchmark catalyst (Figure 30) at the high K_2O loading of 10 wt.%.

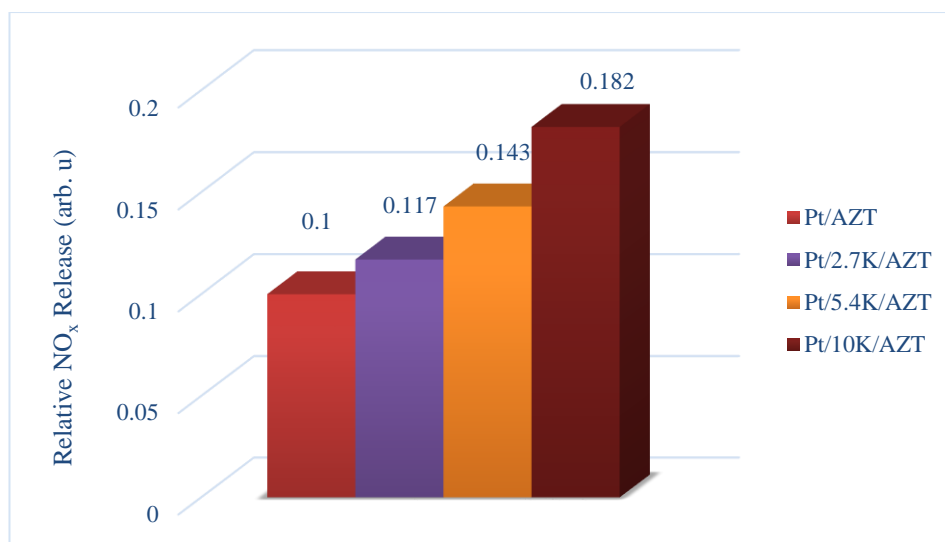


Figure 31 : Surface area normalized NSC values of K_2O loaded AZT catalysts obtained from integrated NO_x TPD signals.

3.3.1.2 NO_x TPD Analysis of Multi Storage Domain Materials

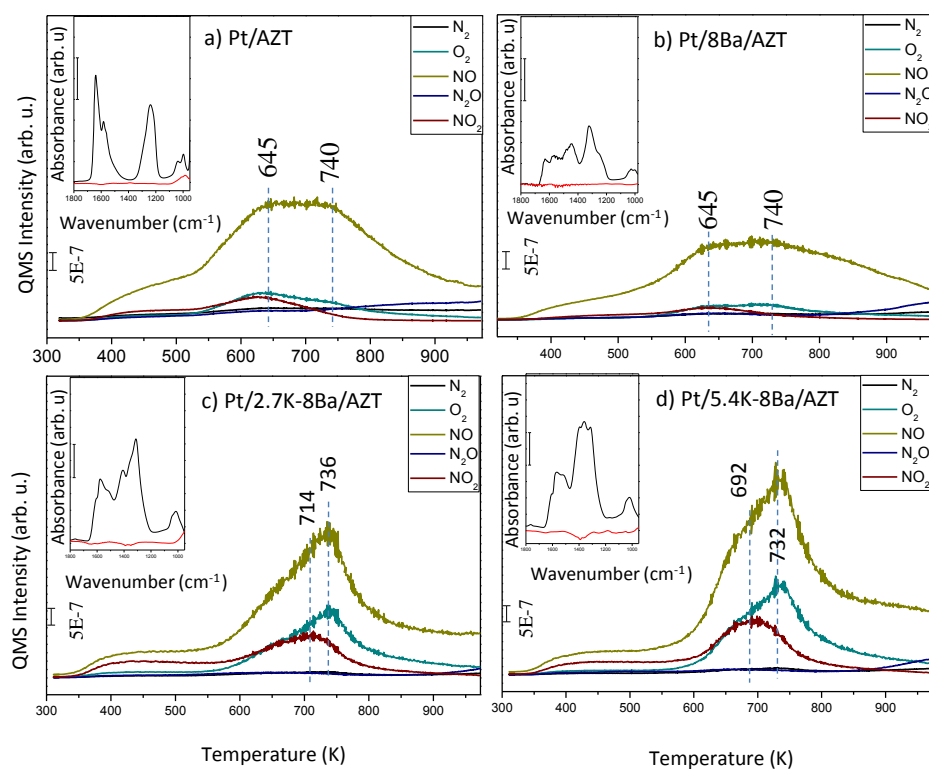


Figure 32 : NO_x TPD profiles for a) Pt/AZT, b) Pt/8Ba/AZT c) Pt/2.7K-8Ba/AZT, d) Pt/5.4K-8Ba/AZT samples after saturation with 5 Torr NO₂ (g) at 323 K for 10 min. The inset spectra in each panel represent in-situ FTIR spectra before (black) and after (red) TPD analysis.

In Figure 32, NO_x TPD profiles of Pt/AZT, Pt/8Ba/AZT, Pt/2.7K-8Ba/AZT and Pt/5.4K-8Ba/AZT are given. Probably one of the most striking features of the NO_x desorption profiles of multi-storage domain catalysts with low (8wt.%) BaO loading is the suppression of the low-temperature NO_x desorption pathways. This observation indicates the increased stability of the stored nitrate species in the co-presence of BaO and K₂O shifting the desorption temperatures to higher values. As

can be seen from the insets of Figure 32, all corresponding materials are fully regenerated upon heating at 973 K.

NO_x adsorption capability of multi storage domain samples with 8wt.% BaO loading are shown in Figure 33 in comparison to Pt/AZT and Pt/8Ba/AZT samples. Data given in Figure 33 clearly show that Pt/5.4K-8Ba/AZT sample has a slightly higher NSC in comparison to Pt/8Ba/AZT sample. Surface area normalized NSC of these samples can be ranked as Pt/5.4K-8Ba/AZT > Pt/8Ba/AZT > Pt/2.7K-8Ba/AZT > Pt/AZT.

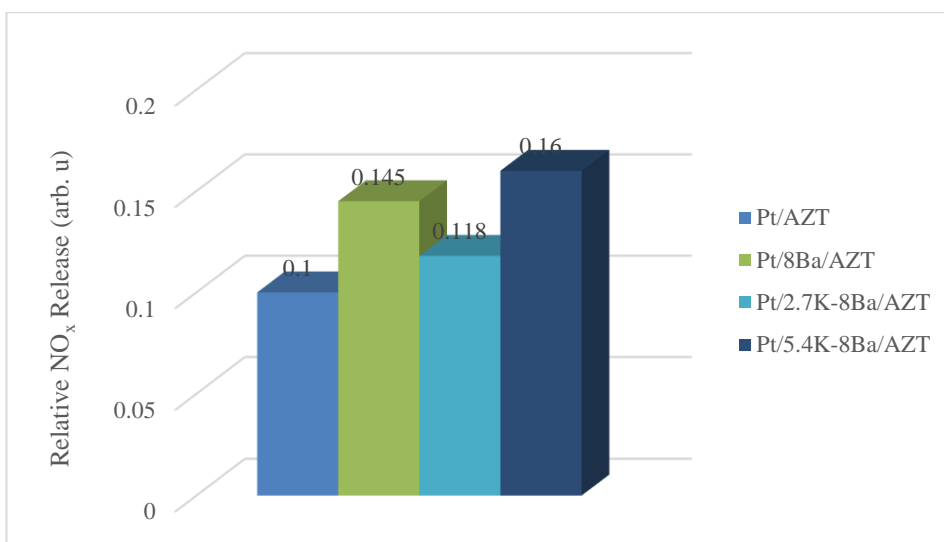


Figure 33 : Surface area normalized NSC values of K₂O-BaO co-loaded AZT catalysts containing 8 wt.% BaO obtained from integrated NO_x TPD signals.

In Figure 34, NO_x TPD profiles K₂O-BaO co-loaded AZT catalysts containing 20 wt.% BaO samples were shown. It is apparent that for these samples, NO_x desorption temperatures shift further to higher temperatures as compared to all of the other catalysts discussed earlier where the NO_x desorption features below

700 K are significantly suppressed. This points to the increased thermal stability of nitrates on the Pt/2.7K-20Ba/AZT and Pt/5.4K-20Ba/AZT samples.

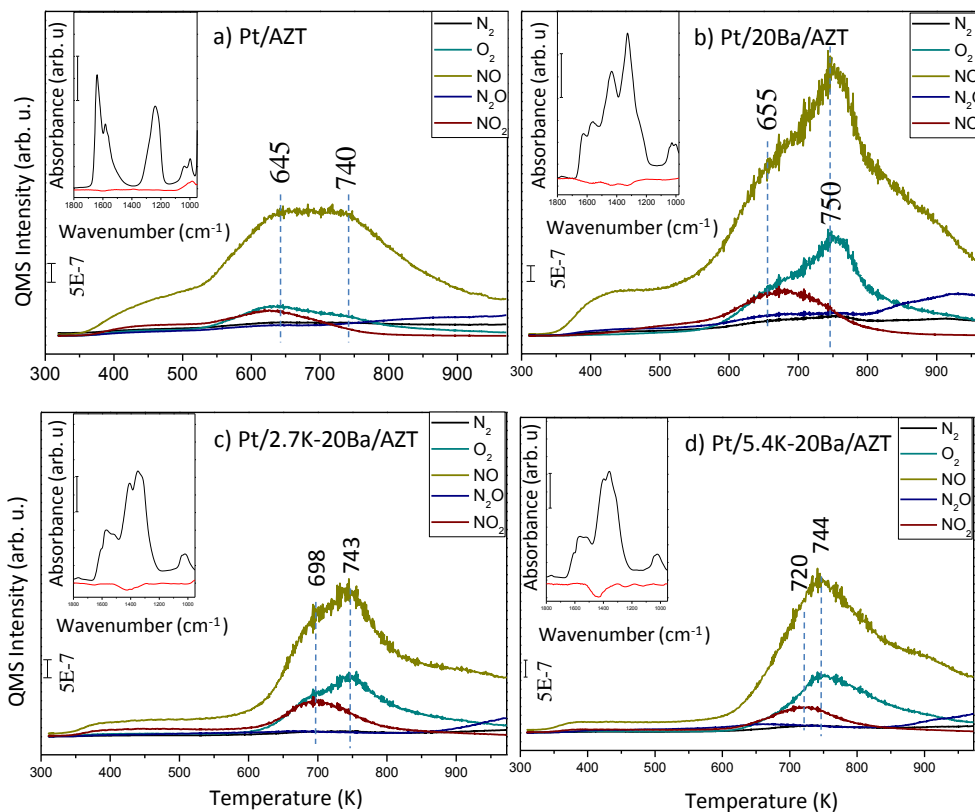


Figure 34 : NO_x TPD profiles for a) Pt/AZT, b) Pt/20Ba/AZT c) Pt/2.7K-20Ba/AZT, d) Pt/5.4K-20Ba/AZT samples after saturation with 5 Torr NO₂ (g) at 323 K for 10 min. The inset spectra in each panel represent *in-situ* FTIR spectra before (black) and after (red) TPD analysis.

Figure 35 represents calculated total relative NO_x release after TPD experiments for Pt/AZT, Pt/20Ba/AZT, Pt/2.7K-20Ba/AZT and Pt/5.4K-20Ba/AZT catalysts normalized using SSA values. It is clear that Pt/20Ba/AZT and Pt/5.4K-20Ba/AZT samples have relatively similar NSC, while the latter is also capable of storing nitrates at higher temperatures.

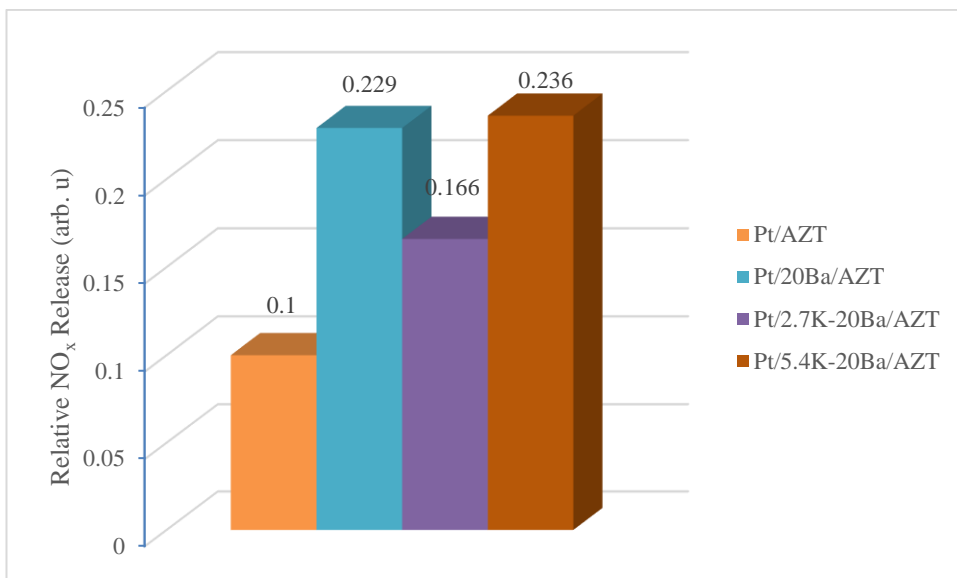


Figure 35 : Surface area normalized NSC values of K₂O-BaO co-loaded AZT catalysts containing 20 wt.% BaO obtained from integrated NO_x TPD signals.

In order to emphasize the capability of the multi-storage domain AZT systems towards storing nitrates at higher temperatures, we have also computed the SSA normalized NO_x desorption at T < 573 K (Figure 36). Data given in Figure 36 illustrates the relative amount “NO_x-slip” at low temperatures. Thus, as low-temperature “NO_x-slip” increases, capability of the catalyst to store nitrates at elevated temperature decreases. As can be seen from Figure 36, low-temperature “NO_x-slip” is minimum for the Pt/5.4K-20Ba/AZT catalyst, suggesting a wider thermal operational window for this particular material than that of the Pt/20Ba/AZT and the Pt/20Ba/Al benchmark catalyst [64, 80].

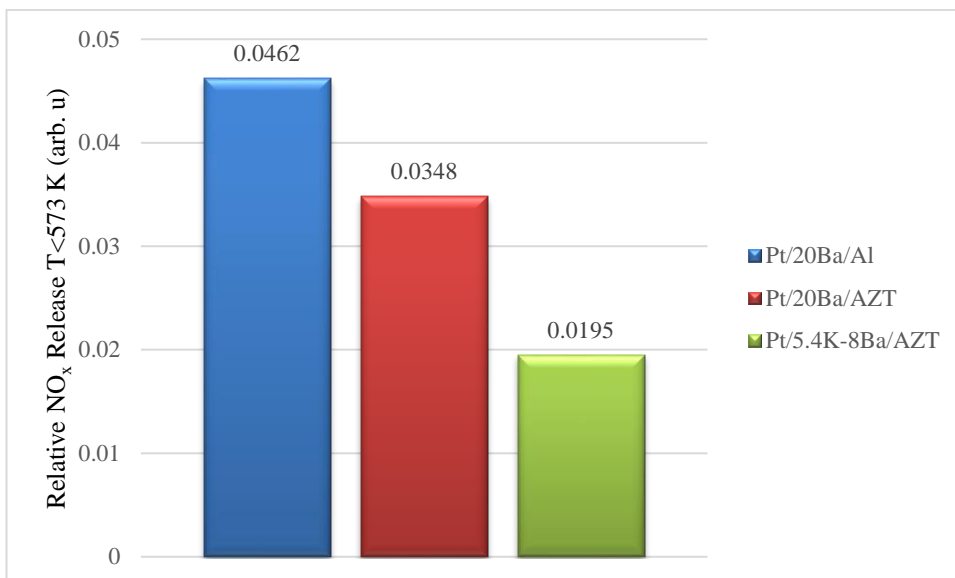


Figure 36 : Surface area normalized relative “NO_x-slip” values of K₂O-BaO co-loaded AZT catalysts at T < 573 K, containing 20 wt.% BaO obtained from integrated NO_x TPD signals.

3.3.2 SO_x TPD Analysis

Thermal regeneration of the sulfated catalysts in the absence of a reducing agent was studied using the TPD technique. For the sulfation experiments, the activated surface of the catalyst was exposed to 2 Torr SO_x (g) (SO₂:O₂ = 1:10) at 673 K for 30 min. After system was outgassed at 10⁻⁶ Torr to remove weakly physisorbed species on the surface of the catalyst, FTIR spectrum was recorded at 323 K and TPD experiment was performed. TPD profiles of these catalysts were recorded at m/z= 32 and 64 that correspond to O₂ and SO₂, respectively. After the TPD experiment, FTIR spectrum was acquired to analyze the residual surface species.

3.3.2.1 SO_x TPD Analysis of Single Storage Domain Materials

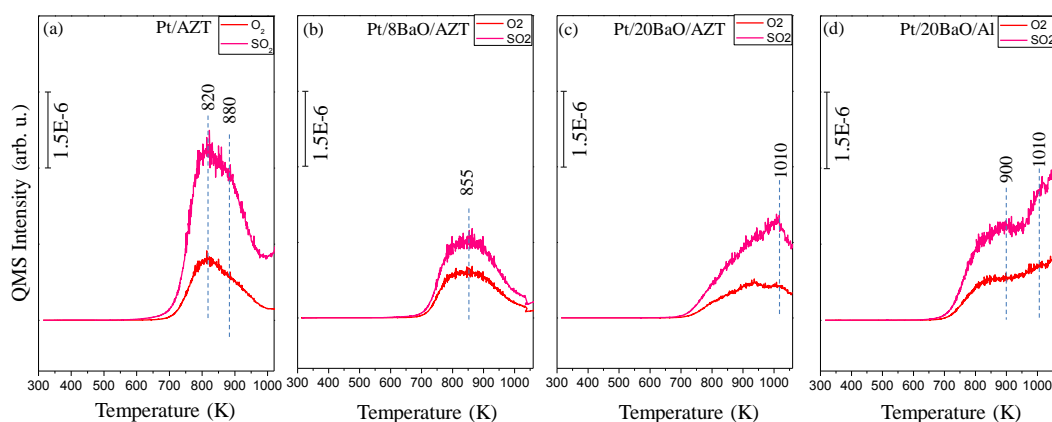


Figure 37 : SO_x TPD profiles for a) Pt/AZT, b) Pt/8Ba/AZT c) Pt/20Ba/AZT, d) Pt/20Ba/Al samples after 2 Torr SO_x adsorption at 673 K for 30 min.

SO_x TPD profiles of the Pt/AZT, Pt/8Ba/AZT, Pt/20Ba/AZT and Pt/20Ba/Al (benchmark) samples, were shown in Figure 37 revealing the thermal regeneration ability after sulfur poisoning in the absence of a reducing agent. These TPD profiles indicate that adsorbed sulfate/sulfite species on surface of the catalysts are highly stable. Therefore, the thermal regeneration temperatures of the poisoned samples are relatively high ($T > 800$ K). The QMS intensity of Pt/AZT sample was higher than that of the other catalysts, which means that the amount of adsorbed sulfate/sulfite species on Pt/AZT surface was higher within the investigated temperature window. Excess BaO loaded AZT samples causes a shift in the decomposition temperatures to 900-1000 K. TPD profile of Pt/20Ba/AZT sample points out to the fact that regeneration process continues to occur at $T > 1050$ K. Note that 1050 K is the ultimate temperature that can be achieved in the current TPD setup.

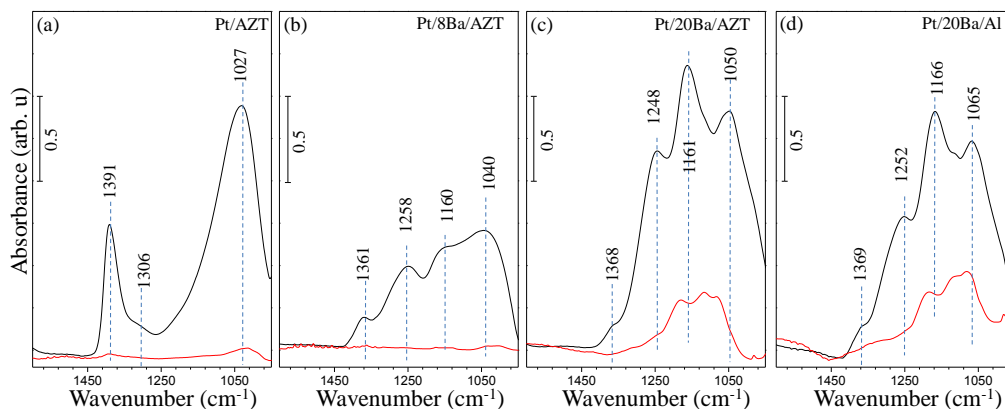


Figure 38 : *In-situ* FTIR spectra corresponding to residual sulfur content on Pt/AZT, Pt/8Ba/AZT, Pt/20Ba/AZT and Pt/20Ba/Al samples before (black) and after (red) SO_x TPD experiments.

Residual sulfur analysis of Pt/AZT and BaO loaded on AZT samples were investigated by means of *in-situ* FTIR spectroscopy. By acquiring FTIR spectra before and after TPD experiments, completion of the sulfur regeneration processes were investigated. According to Figure 38, adsorbed S-related species on Pt/AZT surface were relatively weakly bounded in comparison BaO loaded AZT samples and all of them can be desorbed from the surface at $T < 1050$ K.. AZT samples with high (20 wt.%) BaO loading yields stronger adsorption sites for SO_x yielding residual sulfate/sulfite species remaining on Pt/20Ba/AZT and Pt/20Ba/Al surfaces after the TPD experiments. This can be attributed to the presence of a large amount of thermally stable bulk sulfates on these surfaces which are resilient to thermal regeneration requiring temperatures higher than 1050 K for decomposition/desorption.

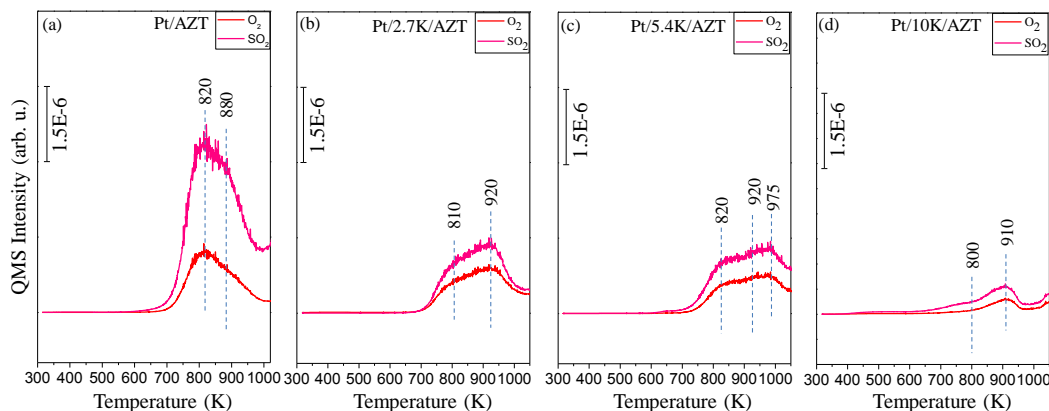


Figure 39 : TPD profiles for a) Pt/AZT, b) Pt/2.7K/AZT c) Pt/5.4K/AZT, d) Pt/10K/AZT samples after 2 Torr SO_x adsorption at 673 K for 30 min.

Identical set of experiments were also performed for K₂O based AZT catalysts and shown in Figure 39. Figure 39a corresponds to sulfur poisoned TPD analysis profile of Pt/AZT sample to analyze the effect of K₂O loading on AZT support. Low, moderate and high K₂O loading samples had relatively smaller SO_x desorption intensities in comparison that of Pt/AZT sample. The spectral line shape of potassium oxide loading AZT samples propose two different desorption signals at T < 1050 K. desorption maxima was located at *ca.* 800 K and 900 K. Furthermore, in Figure 34b-d, it can be seen that SO_x desorption of the catalysts proceed at T > 1050 K as evident by the presence of an upward desorption tail at 1050 K.

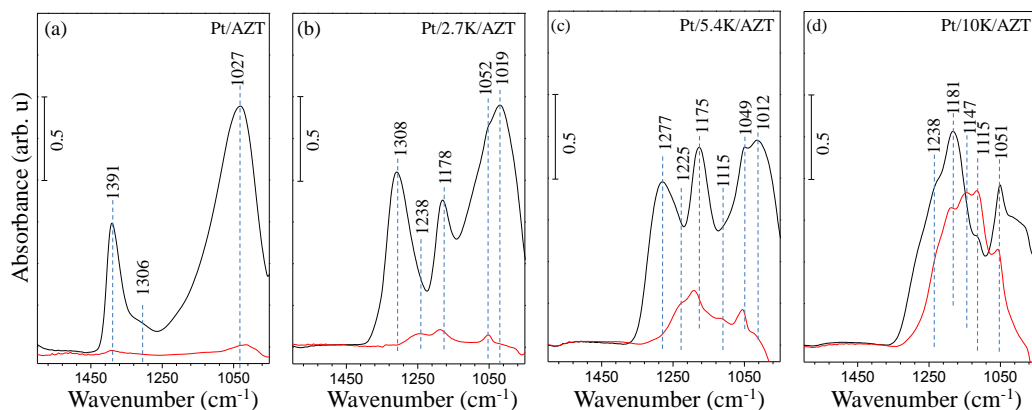


Figure 40 : *In-situ* FTIR spectra corresponding to residual sulfur content on Pt/AZT, Pt/2.7K/AZT, Pt/5.4K/AZT and Pt/10K/AZT samples before (black) and after (red) SO_x TPD experiment.

In Figure 40, FTIR spectra that are taken before and after TPD analysis of Pt/AZT, Pt/2.7K/AZT, Pt/5.4K/AZT and Pt/10K/AZT are illustrated. As mentioned before, SO_x species adsorbed on potassium oxide incorporated AZT support are thermally stable. Thus, red spectra in Figures 40b-d reveal significant amount of sulfite/sulfate groups on the surfaces of the catalysts after the TPD experiments. It can also be noticed that with increasing K₂O loading, thermally stable S- related features increase since the increasing potassium oxide loading leads to the generation of stable bulk-like sulfate species.

Thus, it can be stated that the SO_x adsorption strength of the K₂O based AZT catalysts increases in the following order:

$$\text{Pt/AZT} < \text{Pt/2.7K/AZT} < \text{Pt/5.4K/AZT} < \text{Pt/10K/AZT}.$$

3.3.2.2 SO_x TPD Analysis of Multi Storage Domain Materials

SO_x TPD performance of K₂O and BaO co-impregnated AZT samples were measured and compared to that of the BaO based AZT samples. Figure 41 illustrates TPD desorption signals of sulfur poisoned Pt/AZT, Pt/8Ba/AZT, Pt/2.7K-8Ba/AZT and Pt/5.4K-8Ba/AZT samples. It is apparent that the increase in the K₂O loading leads to an increase in the SO_x desorption peaks and leads to incomplete thermal regeneration at T < 1050 K. Extent of the completion of the SO_x thermal regeneration was further analyzed with *in-situ* FTIR spectroscopy (Figure 42).

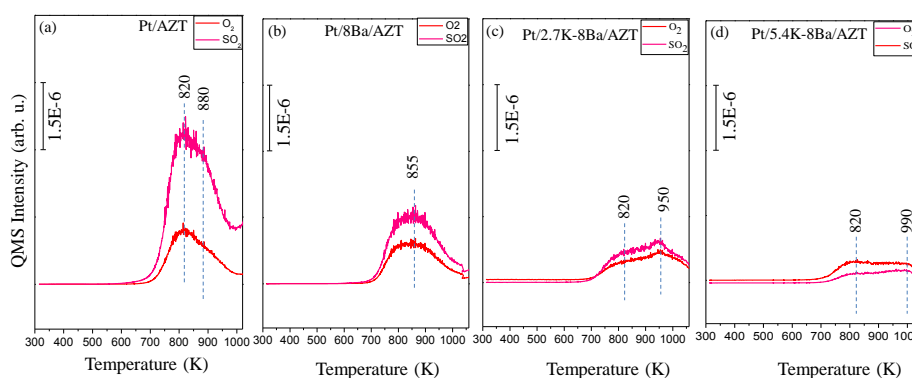


Figure 41 : TPD profiles for a) Pt/AZT, b) Pt/8Ba/AZT c) Pt/2.7K-8Ba/AZT, d) Pt/5.4K-8Ba/AZT samples after 2 Torr SO_x adsorption at 673 K for 30 min.

Figure 42 presents residual sulfur analysis of Pt/AZT, Pt/8Ba/AZT, Pt/2.7K-8Ba/AZT and Pt/5.4K-8Ba/AZT samples *via in-situ* FTIR spectroscopy. Although Pt/AZT and Pt/8Ba/AZT samples were completely regenerated after TPD analysis, potassium oxide and baria co-loaded AZT catalysts could not be fully regenerated. When we compare Pt/2.7K-8Ba/AZT and Pt/5.4K-8Ba/AZT with the Pt/20Ba/Al benchmark catalyst (Figure 37d and Figure 38d), thermal stability of sulfur species

on these surfaces in the absence of a reducing agent seem to be rather comparable. Due to the lack of sufficient NSC, Pt/2.7K-8Ba/AZT cannot be considered as a promising NSR catalyst. On the other hand, Pt/5.4K-8Ba/AZT catalyst has comparable thermal SO_x regeneration capability (Figure 42 d and Figure 38 d) and NSC (Figure 29 and Figure 33) to the Pt/20Ba/Al benchmark catalyst and has even superior SO_x reduction characteristics in the presence of a reducing agent (Figure 26c and 24d).

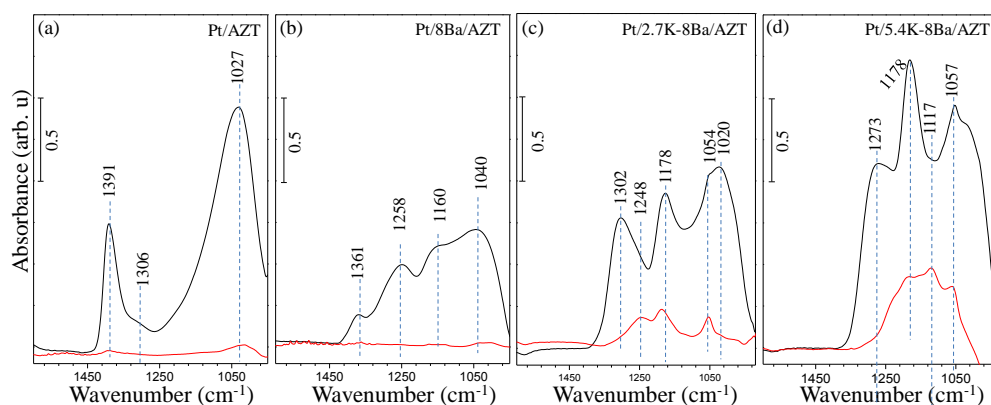


Figure 42 : FTIR spectra corresponding to residual sulfur content on Pt/AZT, Pt/8Ba/AZT, Pt/2.7K-8Ba/AZT and Pt/5.4K-8Ba/AZT and samples before (black) and after (red) SO_x TPD experiments.

Figure 43 demonstrates the SO_x TPD profiles of poisoned Pt/AZT, Pt/20Ba/AZT, Pt/2.7K-20Ba/AZT and Pt/5.4K-20Ba/AZT samples. These spectra reveal the need for very high decomposition temperatures for the thermal SO_x regeneration in the absence of a reducing agent. Adsorbed SO_x species on Pt/2.7K-20Ba/AZT and Pt/5.4K-20Ba/AZT surface are particularly stable as can be seen in Figures 43c-d, presenting very insignificant amount of SO_x desorption at T <1050 K. Adsorbed SO_x species cannot be fully removed from these surfaces.

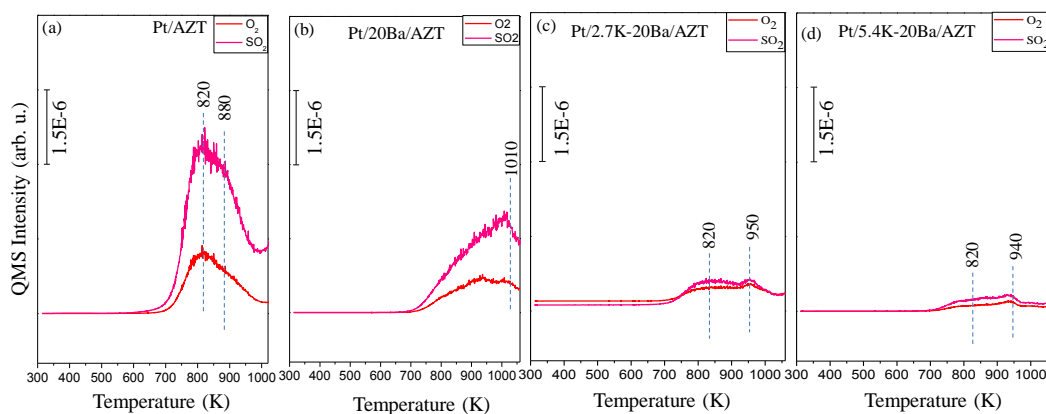


Figure 43 : TPD profiles for a) Pt/AZT, b) Pt/20Ba/AZT c) Pt/2.7K-20Ba/AZT, d) Pt/5.4K-20Ba/AZT samples after 2 Torr SO_x adsorption at 673 K for 30 min.

Residual SO_x analysis of Pt/AZT, Pt/20Ba/AZT, Pt/2.7K-20Ba/AZT and Pt/5.4K-20Ba/AZT samples are demonstrated in Figure 44. While sulfur removal was completely achieved for the Pt/AZT sample, high loadings of basic oxides on AZT failed to provide satisfactory sulfur regeneration performance. Increasing basic oxide loading (K_2O and BaO) causes increasing SO_x stability on the surface. Although basic storage domains are important for NO_x storage capability of the sample, their excessive utilization leads to severe poisoning and poor regeneration.

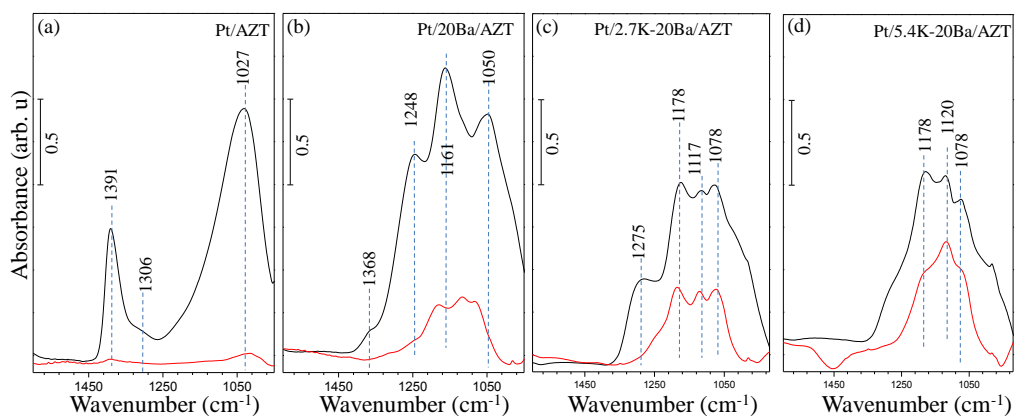


Figure 44 : *In-situ* FTIR spectra corresponding to residual sulfur content on Pt/AZT, Pt/20Ba/AZT, Pt/2.7K-20Ba/AZT and Pt/5.4K-20Ba/AZT and samples before (black) and after (red) SO_x TPD experiments.

Chapter 4

Conclusion

In the current work, NO_x Storage Reduction (NSR) catalysts was promoted with different mixed oxides and basic storage domains. Al₂O₃/ZrO₂/TiO₂ ternary mixed oxide was used as a support material of the currently utilized advanced NSR catalytic architecture. As a storage material, BaO and/or K₂O were loaded on the AZT samples and all of the catalysts were functionalized with Pt redox sites for NO_x/SO_x oxidation and reduction.

For structural characterization, XRD and BET analysis and functional characterization experiments were performed for each catalyst and all of the measurements were compared with that of the Pt/20Ba/Al benchmark catalyst. NO_x saturation/reduction and SO_x saturation/reduction experiments were analyzed by means of *in-situ* FTIR spectroscopy. In addition to this, the NO_x and SO_x TPD experiments were carried out on these catalysts to obtain insight regarding NSC and SO_x regeneration characteristics. Our major findings can be summarized as follows:

- Pt/AZT sample has a highly amorphous structure with poor Pt dispersion and baria incorporation enhances Pt dispersion by decreasing the average Pt particle size.
- Multi storage domain samples have better Pt dispersion than single storage domain AZT catalysts.

- According to BET analysis, specific surface area (SSA) of Pt/AZT is 191 m²/g and increasing K₂O and BaO loadings decreases SSA values of the catalyst. Pt/5.4K-8Ba/AZT sample reveals an optimum SSA with sufficient storage sites.
- Adsorbed NO_x features on surface of the catalysts change when different basic oxides were used. Increasing the storage domain loading leads to the formation of stable bulk-like nitrates.
- In the presence of a reducing agent such as H₂ (g), Pt/5.4 K-8Ba/AZT sample can be fully regenerated at 573 K, while Pt/20Ba/AZT or Pt/20Ba/Al benchmark catalyst could not be completely regenerated under identical conditions.
- Increasing the basic storage domain loading in the catalyst formulation results in the formation of thermally stable bulk-like sulfate/sulfite species on surfaces of these catalysts.
- In the absence of a reducing agent, Pt/20Ba/AZT and Pt/5.4K-20Ba/AZT samples can perform thermal SO_x regeneration at 773 K in vacuum while Pt/20Ba/Al the benchmark catalyst requires a temperature of 973 K.
- Single-storage domain AZT systems containing K₂O have poor thermal SO_x regeneration capability in the absence of a reducing agent (*i.e.* in vacuum). However, in the presence of a reducing agent such as H₂ (g), they can outperform BaO-based single storage domain catalysts in terms of SO_x reduction/regeneration.

- Based on NO_x TPD analysis, relative SSA normalized NSC of the BaO-based single storage domain catalysts and K₂O-based single storage domain catalysts can be ranked as: Pt/20Ba/AZT>Pt/20Ba/Al>Pt/8Ba/AZT>Pt/AZT and Pt/10K/AZT>Pt/5.4K/AZT >Pt/2.7K/AZT > Pt/AZT, respectively.
- Stored nitrate/nitrite species on the surfaces of all of the investigated catalysts can be completely removed from the surfaces after the TPD experiments (*i.e.* after heating up 973 K under vacuum).
- Based on NO_x TPD analysis, SSA normalized NSC of the samples decrease in the following order: Pt/5.4K-20Ba/AZT > Pt/20Ba/Al > Pt/2.7K-8Ba/AZT>Pt/5.4K-8Ba/AZT>Pt/8Ba/AZT>Pt/2.7K-8Ba/AZT.
- Pt/5.4K-8Ba/AZT catalyst show rather comparable NSC to that of the benchmark catalyst with superior SO_x regeneration characteristics. Furthermore, this advanced NSR architecture has also a wider thermal NO_x storage window than can allow the operation of these catalysts in a broader temperature regime suitable for a variety of urban/rural driving cycles and engine power.
- Operational temperature window, NSC and sulfur tolerance of the NSR catalysts can be fine-tuned by the rational design of the surface chemistry of the catalyst at the nanometer scale.

Bibliography

- [1] (2013). *Cars, Trucks, and Air Pollution*. Available: <http://www.ucsusa.org/clean-vehicles/vehicles-air-pollution-and-human-health/cars-trucks-air-pollution#.V1rZ4NJ95di>
- [2] (2016). *Emissions of air pollutants from transport* Available: <http://www.eea.europa.eu/data-and-maps/indicators/transport-emissions-of-air-pollutants-8/transport-emissions-of-air-pollutants-3/#emissions-of-air-pollutants-from-transport>
- [3] (2016). *Air pollution: a global assessment of exposure and burden of disease*. Available: <http://www.who.int/mediacentre/news/releases/2016/deaths-attributable-to-unhealthy-environments/en/>
- [4] (2016). *Mortality Due To Air Pollution* Available: <http://www.who.int/mediacentre/factsheets/fs313/en/>
- [5] J. G. Nunan, H. J. Robota, M. J. Cohn, and S. A. Bradley, "Physicochemical properties of Ce-containing three-way catalysts and the effect of Ce on catalyst activity," *Journal of Catalysis*, vol. 133, pp. 309-324, 1992.
- [6] R. M. Heck, R. J. Farrauto, and S. T. Gulati, *Catalytic air pollution control: commercial technology*: John Wiley & Sons, 2009.
- [7] F. Basile, G. Fornasari, A. Grimandi, M. Livi, and A. Vaccari, "Effect of Mg, Ca and Ba on the Pt-catalyst for NO_x storage reduction," *Applied Catalysis B: Environmental*, vol. 69, pp. 58-64, 2006.
- [8] Q. Wang, J. H. Sohn, and J. S. Chung, "Thermally stable Pt/K₂Ti₂O₅ as high-temperature NO_x storage and reduction catalyst," *Applied Catalysis B: Environmental*, vol. 89, pp. 97-103, 2009.
- [9] J. E. Parks, "Less costly catalysts for controlling engine emissions," *Science*, vol. 327, pp. 1584-1585, 2010.
- [10] L. Landong, C. Jixin, Z. Shujuan, Z. Fuxiang, G. Najjia, W. Tianyou, *et al.*, "Selective catalytic reduction of nitrogen oxides from exhaust of lean burn engine over in-situ synthesized Cu-ZSM-5/cordierite," *Environmental science & technology*, vol. 39, pp. 2841-2847, 2005.
- [11] R. D. Clayton, M. P. Harold, and V. Balakotaiah, "NO_x storage and reduction with H₂ on Pt/BaO/Al₂O₃ monolith: Spatio-temporal resolution of

- product distribution," *Applied Catalysis B: Environmental*, vol. 84, pp. 616-630, 2008.
- [12] W. S. Epling, L. E. Campbell, A. Yezerets, N. W. Currier, and J. E. Parks, "Overview of the fundamental reactions and degradation mechanisms of NO_x storage/reduction catalysts," *Catalysis Reviews*, vol. 46, pp. 163-245, 2004.
- [13] P. S. Monks, C. Granier, S. Fuzzi, A. Stohl, M. L. Williams, H. Akimoto, *et al.*, "Atmospheric composition change – global and regional air quality," *Atmospheric Environment*, vol. 43, pp. 5268-5350, 2009.
- [14] F. Klingstedt, K. Arve, K. Eränen, and D. Y. Murzin, "Toward improved catalytic low-temperature NO_x removal in diesel-powered vehicles," *Accounts of chemical research*, vol. 39, pp. 273-282, 2006.
- [15] Q. Schiermeier, "The science behind the Volkswagen emissions scandal," in *Nat. News*, ed, 2015.
- [16] Y. Yokomichi, T. Yamabe, T. Kakumoto, O. Okada, H. Ishikawa, Y. Nakamura, *et al.*, "Theoretical and experimental study on metal-loaded zeolite catalysts for direct NO_x decomposition," *Applied Catalysis B: Environmental*, vol. 28, pp. 1-12, 2000.
- [17] H. L. Fang and H. F. M. DaCosta, "Urea thermolysis and NO_x reduction with and without SCR catalysts," *Applied Catalysis B: Environmental*, vol. 46, pp. 17-34, 2003.
- [18] V. Houel, P. Millington, R. Rajaram, and A. Tsolakis, "Fuel effects on the activity of silver hydrocarbon-SCR catalysts," *Applied Catalysis B: Environmental*, vol. 73, pp. 203-207, 2007.
- [19] J. Li, R. Ke, W. Li, and J. Hao, "A comparison study on non-thermal plasma-assisted catalytic reduction of NO by C₃H₆ at low temperatures between Ag/USY and Ag/Al₂O₃ catalysts," *Catalysis Today*, vol. 126, pp. 272-278, 2007.
- [20] S. i. Matsumoto, Y. Ikeda, H. Suzuki, M. Ogai, and N. Miyoshi, "NO_x storage-reduction catalyst for automotive exhaust with improved tolerance against sulfur poisoning," *Applied Catalysis B: Environmental*, vol. 25, pp. 115-124, 2000.
- [21] 胡准, 孙科强, and 徐柏庆, "Pt-BaO 催化剂的 NO_x 储存-还原化学及结构-性能关系," *Chinese Journal of Catalysis*, vol. 32, pp.17-26. 2011.

- [22] S. Roy and A. Baiker, "NO_x Storage–Reduction Catalysis: From Mechanism and Materials Properties to Storage–Reduction Performance," *Chemical Reviews*, vol. 109, pp. 4054-4091, 2009.
- [23] D. Bhatia, R. W. McCabe, M. P. Harold, and V. Balakotaiah, "Experimental and kinetic study of NO oxidation on model Pt catalysts," *Journal of Catalysis*, vol. 266, pp. 106-119, 2009.
- [24] J. Xu, M. P. Harold, and V. Balakotaiah, "Microkinetic modeling of steady-state NO/H₂/O₂ on Pt/BaO/Al₂O₃ NO_x storage and reduction monolith catalysts," *Applied Catalysis B: Environmental*, vol. 89, pp. 73-86, 2009.
- [25] A. Smeltz, R. B. Getman, W. Schneider, and F. Ribeiro, "Coupled theoretical and experimental analysis of surface coverage effects in Pt-catalyzed NO and O₂ reaction to NO₂ on Pt (111)," *Catalysis Today*, vol. 136, pp. 84-92, 2008.
- [26] S. Mulla, N. Chen, W. Delgass, W. Epling, and F. Ribeiro, "NO₂ inhibits the catalytic reaction of NO and O₂ over Pt," *Catalysis Letters*, vol. 100, pp. 267-270, 2005.
- [27] L. Olsson and E. Fridell, "The Influence of Pt Oxide Formation and Pt Dispersion on the Reactions NO₂ ⇌ NO + 1/2O₂ over Pt/Al₂O₃ and Pt/BaO/Al₂O₃," *Journal of Catalysis*, vol. 210, pp. 340-353, 2002.
- [28] R. L. Muncrief, P. Khanna, K. S. Kabin, and M. P. Harold, "Mechanistic and kinetic studies of NO_x storage and reduction on Pt/BaO/Al₂O₃," *Catalysis today*, vol. 98, pp. 393-402, 2004.
- [29] L. Olsson, H. Persson, E. Fridell, M. Skoglundh, and B. Andersson, "A Kinetic Study of NO Oxidation and NO_x Storage on Pt/Al₂O₃ and Pt/BaO/Al₂O₃," *The Journal of Physical Chemistry B*, vol. 105, pp. 6895-6906, 2001.
- [30] G. Mestl, S. Xie, Michael, P. Rosynek, and J. H. Lunsford, "In Situ Raman evidence for a barium solid state phase that is active in nitric oxide decomposition: influence of preparation parameters," in *Studies in Surface Science and Catalysis*. vol. Volume 118, P. A. J. R. M. J. A. M. P. G. B. Delmon and G. Poncelet, Eds., ed: Elsevier, 1998, pp. 459-467.
- [31] E. Fridell, M. Skoglundh, B. Westerberg, S. Johansson, and G. Smedler, "NO_x storage in barium-containing catalysts," *Journal of Catalysis*, vol. 183, pp. 196-209, 1999.
- [32] G. Glazneva, A. Davydov, I. Sazonova, Y. Shchekochikhin, and N. Keier, "IR spectroscopic study of interaction of nitric-oxide with carbon-monoxide on Fe₂O₃," *Kinetics And Catalysis*, vol. 19, pp. 801-806, 1978.

- [33] A. Davydov, "IR spectroscopy applied to surface chemistry of oxides," ed: Nauka, Novosibirsk, 1984.
- [34] A. A. Davydov and N. Sheppard, *Molecular spectroscopy of oxide catalyst surfaces* vol. 690: Wiley Chichester, 2003.
- [35] Z. Say, M. Tohumeken, and E. Ozensoy, "NO_x storage and reduction pathways on zirconia and titania functionalized binary and ternary oxides as NO_x storage and reduction (NSR) systems," *Catalysis Today*, vol. 231, pp. 135-144, 2014.
- [36] H. Arai and M. Machida, "Removal of NO_x through sorption-desorption cycles over metal oxides and zeolites," *Catalysis today*, vol. 22, pp. 97-109, 1994.
- [37] M. Machida, N. Masuda, and T. Kijima, "Sorption-desorption properties of nitric oxide over La_{2-x}Sr_{1+x}Cu₂O_{6-δ} (0 ≤ x ≤ 2)," *Journal of Materials Chemistry*, vol. 9, pp. 1369-1374, 1999.
- [38] K. Eguchi, T. Kondo, T. Hayashi, and H. Arai, "Sorption of nitrogen oxides on MnO_y-ZrO₂ and Pt-ZrO₂-Al₂O₃," *Applied Catalysis B: Environmental*, vol. 16, pp. 69-77, 1998.
- [39] S. M. Park, J. W. Park, H.-P. Ha, H.-S. Han, and G. Seo, "Storage of NO₂ on potassium oxide co-loaded with barium oxide for NO_x storage and reduction (NSR) catalysts," *Journal of molecular catalysis A: chemical*, vol. 273, pp. 64-72, 2007.
- [40] F. Prinetto, M. Manzoli, S. Morandi, F. Frola, G. Ghiotti, L. Castoldi, *et al.*, "Pt- K/Al₂O₃ NSR Catalysts: Characterization of Morphological, Structural and Surface Properties," *The Journal of Physical Chemistry C*, vol. 114, pp. 1127-1138, 2009.
- [41] K. Yamamoto, R. Kikuchi, T. Takeguchi, and K. Eguchi, "Development of NO sorbents tolerant to sulfur oxides," *Journal of Catalysis*, vol. 238, pp. 449-457, 2006.
- [42] T. Kanazawa, "Development of hydrocarbon adsorbents, oxygen storage materials for three-way catalysts and NO_x storage-reduction catalyst," *Catalysis Today*, vol. 96, pp. 171-177, 2004.
- [43] K. Ito, S. Kakino, K. Ikeue, and M. Machida, "NO adsorption/desorption property of TiO₂-ZrO₂ having tolerance to SO₂ poisoning," *Applied Catalysis B: Environmental*, vol. 74, pp. 137-143, 2007.
- [44] Available: <http://chemistry-reference.com/reaction.asp?rxnnum=88>

- [45] M. Happel, A. Desikusumastuti, M. Sobota, M. Laurin, and J. r. Libuda, "Impact of Sulfur Poisoning on the NO_x Uptake of a NO_x Storage and Reduction (NSR) Model Catalyst," *The Journal of Physical Chemistry C*, vol. 114, pp. 4568-4575, 2010.
- [46] K. Wilson, C. Hardacre, C. Baddeley, J. Lüdecke, D. Woodruff, and R. Lambert, "A spectroscopic study of the chemistry and reactivity of SO₂ on Pt {111}: reactions with O₂, CO and C₃H₆," *Surface science*, vol. 372, pp. 279-288, 1997.
- [47] P. Engström, A. Amberntsson, M. Skoglundh, E. Fridell, and G. Smedler, "Sulphur dioxide interaction with NO_x storage catalysts," *Applied Catalysis B: Environmental*, vol. 22, pp. L241-L248, 1999.
- [48] G. Graham, H.-W. Jen, W. Chun, H. Sun, X. Pan, and R. McCabe, "Coarsening of Pt particles in a model NO_x trap," *Catalysis letters*, vol. 93, pp. 129-134, 2004.
- [49] Z. Say, M. Tohumeken, and E. Ozensoy, "Spectroscopic investigation of sulfur-resistant Pt/K₂O/ZrO₂/TiO₂/Al₂O₃ NSR/LNT catalysts," *Catalysis Today*, 2016.
- [50] R. Büchel, R. Strobel, A. Baiker, and S. E. Pratsinis, "Effect of the Proximity of Pt to Ce or Ba in Pt/Ba/CeO₂ Catalysts on NO_x Storage–Reduction Performance," *Topics in Catalysis*, vol. 52, pp. 1709-1712, 2009.
- [51] D. H. Kim, K. Mudiyansele, J. Szányi, H. Zhu, J. H. Kwak, and C. H. F. Peden, "Characteristics of Pt–K/MgAl₂O₄ lean NO_x trap catalysts," *Catalysis Today*, vol. 184, pp. 2-7, 2012.
- [52] M. Takeuchi and S. i. Matsumoto, "NO_x storage-reduction catalysts for gasoline engines," *Topics in catalysis*, vol. 28, pp. 151-156, 2004.
- [53] J. Luo, F. Gao, D. H. Kim, and C. H. Peden, "Effects of potassium loading and thermal aging on K/Pt/Al₂O₃ high-temperature lean NO_x trap catalysts," *Catalysis Today*, vol. 231, pp. 164-172, 2014.
- [54] E. Kayhan, S. M. Andonova, G.S. Şentürk, C. C. Chusuei, and E. Ozensoy, "Fe promoted NO_x storage materials: structural properties and NO_x uptake," *The Journal of Physical Chemistry C*, vol. 114, pp. 357-369, 2009.
- [55] T. Szailer, J. H. Kwak, D. H. Kim, J. C. Hanson, C. H. F. Peden, and J. Szanyi, "Reduction of stored NO_x on Pt/Al₂O₃ and Pt/BaO/Al₂O₃ catalysts with H₂ and CO," *Journal of Catalysis*, vol. 239, pp. 51-64, 2006.

- [56] B. Westerberg and E. Fridell, "A transient FTIR study of species formed during NO_x storage in the Pt/BaO/Al₂O₃ system," *Journal of Molecular Catalysis A: Chemical*, vol. 165, pp. 249-263, 2001.
- [57] L. Lietti, I. Nova, and P. Forzatti, "Role of ammonia in the reduction by hydrogen of NO_x stored over Pt–Ba/Al₂O₃ lean NO_x trap catalysts," *Journal of Catalysis*, vol. 257, pp. 270-282, 2008.
- [58] T. Montanari, L. Castoldi, L. Lietti, and G. Busca, "Basic catalysis and catalysis assisted by basicity: FT-IR and TPD characterization of potassium-doped alumina," *Applied Catalysis A: General*, vol. 400, pp. 61-69, 2011.
- [59] B. I. Mosqueda-Jiménez, A. Lahougue, P. Bazin, V. Harlé, G. Blanchard, A. Sassi, *et al.*, "Operando systems for the evaluation of the catalytic performance of NO_x storage and reduction materials," *Catalysis Today*, vol. 119, pp. 73-77, 2007.
- [60] J.-Y. Luo, M. Al-Harbi, M. Pang, and W. S. Epling, "Spatially resolving LNT desulfation: re-adsorption induced by oxygen storage materials," *Applied Catalysis B: Environmental*, vol. 106, pp. 664-671, 2011.
- [61] K. Hadjiivanov, V. Bushev, M. Kantcheva, and D. Klissurski, "Infrared spectroscopy study of the species arising during nitrogen dioxide adsorption on titania (anatase)," *Langmuir*, vol. 10, pp. 464-471, 1994.
- [62] D. H. Kim, K. Mudiyansele, J. Szanyi, J. H. Kwak, H. Zhu, and C. H. Peden, "Effect of K loadings on nitrate formation/decomposition and on NO_x storage performance of K-based NO_x storage-reduction catalysts," *Applied Catalysis B: Environmental*, vol. 142, pp. 472-478, 2013.
- [63] T. Lesage, J. Saussey, S. Malo, M. Hervieu, C. Hedouin, G. Blanchard, *et al.*, "Operando FTIR study of NO_x storage over a Pt/K/Mn/Al₂O₃-CeO₂ catalyst," *Applied Catalysis B: Environmental*, vol. 72, pp. 166-177, 2007.
- [64] D. Dou and J. Balland, "Impact of alkali metals on the performance and mechanical properties of NO_x adsorber catalysts," SAE Technical Paper 0148-7191, 2002.
- [65] M. Konsolakis and I. Yentekakis, "Strong promotional effects of Li, K, Rb and Cs on the Pt-catalysed reduction of NO by propene," *Applied Catalysis B: Environmental*, vol. 29, pp. 103-113, 2001.
- [66] K. Iwachido, H. Tanada, T. Watanabe, N. Yamada, O. Nakayama, H. Ando, *et al.*, "Development of the NO_x Adsorber Catalyst for Use with High-Temperature Condition," SAE Technical Paper 0148-7191, 2001.

- [67] T. J. Toops, D. B. Smith, and W. P. Partridge, "NO_x adsorption on Pt/K/Al₂O₃," *Catalysis today*, vol. 114, pp. 112-124, 2006.
- [68] J. He, M. Meng, Y. Zha, R. You, and T. Ding, "Prominent enhancement of La₂O₃ addition to the support on the NO_x storage and sulfur-resistance performance of Pt/K/TiO₂-Al₂O₃ lean-burn NO_x trap catalysts," *Materials Chemistry and Physics*, vol. 135, pp. 610-617, 2012.
- [69] M. Waqif, A. Pieplu, O. Saur, J. Lavalley, and G. Blanchard, "Use of CeO₂-Al₂O₃ as a SO₂ sorbent," *Solid State Ionics*, vol. 95, pp. 163-167, 1997.
- [70] M. Kantcheva and E. Z. Ciftlikli, "FTIR Spectroscopic Characterization of NO_x Species Adsorbed on ZrO₂ and ZrO₂-SO₄," *The Journal of Physical Chemistry B*, vol. 106, pp. 3941-3949, 2002.
- [71] G. S. Şentürk, E. I. Vovk, V. I. Zaikovskii, Z. Say, A. M. Soyly, V. I. Bukhtiyarov, *et al.*, "SO_x uptake and release properties of TiO₂/Al₂O₃ and BaO/TiO₂/Al₂O₃ mixed oxide systems as NO_x storage materials," *Catalysis Today*, vol. 184, pp. 54-71, 2012.
- [72] Z. Say, E. I. Vovk, V. I. Bukhtiyarov, and E. Ozensoy, "Influence of ceria on the NO_x reduction performance of NO_x storage reduction catalysts," *Applied Catalysis B: Environmental*, vol. 142, pp. 89-100, 2013.
- [73] C. Sedlmair, K. Seshan, A. Jentys, and J. Lercher, "Studies on the deactivation of NO_x storage-reduction catalysts by sulfur dioxide," *Catalysis Today*, vol. 75, pp. 413-419, 2002.
- [74] H. Abdulhamid, E. Fridell, J. Dawody, and M. Skoglundh, "In situ FTIR study of SO₂ interaction with Pt/BaCO₃/Al₂O₃ NO_x storage catalysts under lean and rich conditions," *Journal of Catalysis*, vol. 241, pp. 200-210, 2006.
- [75] Z. Say, E. I. Vovk, V. I. Bukhtiyarov, and E. Ozensoy, "Enhanced Sulfur Tolerance of Ceria-Promoted NO_x Storage Reduction (NSR) Catalysts: Sulfur Uptake, Thermal Regeneration and Reduction with H₂ (g)," *Topics in Catalysis*, vol. 56, pp. 950-957, 2013.
- [76] Y. Liu, M. Meng, X.-G. Li, L.-H. Guo, and Y.-Q. Zha, "NO_x storage behavior and sulfur-resisting performance of the third-generation NSR catalysts Pt/K/TiO₂-ZrO₂," *chemical engineering research and design*, vol. 86, pp. 932-940, 2008.
- [77] F. M. Hoffmann, "Infrared reflection-absorption spectroscopy of adsorbed molecules," *Surface Science Reports*, vol. 3, pp. 107-192, 1983.

- [78] E. Ozensoy, C. H. Peden, and J. Szanyi, "Model NO_x storage systems: Storage capacity and thermal aging of BaO/θ-Al₂O₃/NiAl (100)," *Journal of Catalysis*, vol. 243, pp. 149-157, 2006.
- [79] G. Mestl, S. Xie, P. Rosynek, and J. H. Lunsford, "In situ Raman evidence for a barium solid state phase that is active in nitric oxide decomposition: influence of preparation parameters," *Studies in Surface Science and Catalysis*, vol. 118, pp. 459-467, 1998.
- [80] L. J. Gill, P. G. Blakeman, M. V. Twigg, and A. P. Walker, "The use of NO_x adsorber catalysts on diesel engines," *Topics in catalysis*, vol. 28, pp. 157-164, 2004.